

Cite this: *Chem. Sci.*, 2023, 14, 1040

All publication charges for this article have been paid for by the Royal Society of Chemistry

Connecting the dots for fundamental understanding of structure–photophysics–property relationships of COFs, MOFs, and perovskites using a Multiparticle Holstein Formalism

Raja Ghosh *^a and Francesco Paesani *^{abc}

Photoactive organic and hybrid organic–inorganic materials such as conjugated polymers, covalent organic frameworks (COFs), metal–organic frameworks (MOFs), and layered perovskites, display intriguing photophysical signatures upon interaction with light. Elucidating structure–photophysics–property relationships across a broad range of functional materials is nontrivial and requires our fundamental understanding of the intricate interplay among excitons (electron–hole pair), polarons (charges), bipolarons, phonons (vibrations), inter-layer stacking interactions, and different forms of structural and conformational defects. In parallel with electronic structure modeling and data-driven science that are actively pursued to successfully accelerate materials discovery, an accurate, computationally inexpensive, and physically-motivated theoretical model, which consistently makes quantitative connections with conceptually complicated experimental observations, is equally important. Within this context, the first part of this perspective highlights a unified theoretical framework in which the electronic coupling as well as the local coupling between the electronic and nuclear degrees of freedom can be efficiently described for a broad range of quasiparticles with similarly structured Holstein-style vibronic Hamiltonians. The second part of this perspective discusses excitonic and polaronic photophysical signatures in polymers, COFs, MOFs, and perovskites, and attempts to bridge the gap between different research fields using a common theoretical construct – the Multiparticle Holstein Formalism. We envision that the synergistic integration of state-of-the-art computational approaches with the Multiparticle Holstein Formalism will help identify and establish new, transformative design strategies that will guide the synthesis and characterization of next-generation energy materials optimized for a broad range of optoelectronic, spintronic, and photonic applications.

Received 7th July 2022
Accepted 9th November 2022

DOI: 10.1039/d2sc03793a

rsc.li/chemical-science

1 Introduction

A fundamental understanding of excited-state phenomena and the elementary mechanisms that govern photophysical and charge transport processes of multifunctional materials is crucial for new scientific breakthroughs and future technological innovations. Fueled by the discovery of polymer-based light emitting diodes (OLEDs),^{1,2} organic materials continue to find increasing commercial value, with a broad range of applications in photovoltaics,^{3–8} organic spintronics,^{9–12} field effect

transistors,^{13–16} wearable technology,^{16–19} flexible displays,^{20–23} photolithography,^{24,25} and chemosensors and bioprobes.^{4,26,27}

In addition to traditional one-dimensional semiconducting polymers, the discovery of 2D covalent organic frameworks (COFs) in 2005 (ref. 28) has sparked renewed interest in organic electronics. COFs represent an emerging class of porous organic materials that offer a range of unique advantages compared to traditional polymeric materials, such as morphological precision and positional control of diverse functional building blocks.^{28–45} Tremendous efforts are currently focused on taking advantage of the structural diversity, crystallinity, and porosity of various COF structures for potential cutting-edge applications in biomedicine and bioimaging,^{46–50} drug and gene delivery,^{51–54} gas and energy storage,^{55–58} photocatalysis,^{59,60} and ion conduction.^{61,62} Despite the presence of intrinsic porosity, which hinders the efficient movement of charges, COFs have also found applications as semiconducting materials.^{63–72} Energy and charge migration in COFs happen through the

^aDepartment of Chemistry and Biochemistry, University of California, La Jolla, San Diego, California 92093, USA. E-mail: raghosh@ucsd.edu

^bSan Diego Supercomputer Center, University of California, La Jolla, San Diego, California 92093, USA

^cMaterials Science and Engineering, University of California, La Jolla, San Diego, California 92093, USA. E-mail: fpaesani@ucsd.edu



efficient transport of excitons and polarons, respectively, either along the framework backbone (*i.e.*, through bond) or between the π -stacked layers (*i.e.*, through space).

While the facile synthesis of organic materials makes optoelectronic devices inexpensive compared to their inorganic counterparts, structural and conformational disorder often leads to poor conductivity and low mobility.^{73–77} Despite being environmental friendly, organic thermoelectric materials also suffer from low conductivity, Seebeck coefficient, and power factor.⁷⁸ The flexibility of self-assembling organic and inorganic building units to form hybrid organic–inorganic frameworks offers the possibility to combine unique photophysical and electronic properties that are absent in either of the individual building blocks.^{78–80} The combination of high conductivity in the inorganic components with stronger light–matter interactions and higher quantum efficiency of the organic components has proved to be an effective approach which have resulted in much improved electrical, optical, and transport properties.^{80–84} Over the last decade, hybrid organic–inorganic materials, such as metal–organic frameworks (MOFs) and layered perovskites, have received widespread interest for potential applications in various fields of chemistry and materials science.^{85–93} Although MOFs are generally considered as insulating materials, recent studies have reported promising results on the synthesis of intrinsically conducting MOFs.^{94–97} The field of layered perovskites has exploded in the last decade, and two-dimensional (2D) perovskites have emerged as promising candidates for next generation solar cells owing to record power conversion efficiencies which vastly outperform the efficiencies achieved by organic based materials.^{98–102}

The design and synthesis of new materials presents a formidable challenge since chemical manipulation and framework diversity, in principle, allow for myriads of possible structural combinations that enable the fine tuning of optical, electronic, and transport properties. From an experimental viewpoint, establishing efficient synthetic routes for synthesizing novel electronic materials tailored for specific applications remains the main obstacle.

To overcome some of the challenges, computational predictions of new multifunctional materials has been bolstered primarily due to the development of new algorithms and the availability of supercomputers which readily enable the treatment of large number of molecules within a reasonable time frame. Various computational and theoretical approaches, ranging from quantum Monte Carlo (QMC) to molecular dynamics (MD) simulations and density functional theory (DFT) have been utilized to gain new insights into the complicated electronic structure of organic and hybrid materials.¹⁰³ For example, DFT in combination with tight-binding modeling has been extensively employed to investigate the nature of flat bands,¹⁰⁴ electronic structure,^{105,106} structural defects,¹⁰⁷ effects of doping,¹⁰⁸ and interlayer stacking interactions¹⁰⁹ in 2D COFs.

Skillful exploration of data through data-mining and big data approaches as well as electronic structure modeling have greatly benefited the fields of MOFs and perovskites.^{103,110–119} Machine learning and high throughput techniques have been routinely employed to screen the chemical space of hybrid

materials with the goal of proposing new MOF and perovskite structures that are suitable for industrial applications, including but not limited to catalysis,^{120–123} gas storage and separation,¹²⁴ and optoelectronics.^{125–128} While materials modeling based on data-driven approaches has achieved some remarkable success in predicting electronic properties (*e.g.*, band gaps, charge densities, electronic couplings, oscillator strengths, *etc.*), the development of a rigorous theoretical framework that utilizes the calculated properties to make quantitative connections with state-of-the-art ultrafast spectroscopy measurements will further help accelerate materials discovery.

Within this context, the majority of optoelectronic, charge transport and storage, and photonics applications involve the fundamental photophysical process of absorption and emission of light. Excited state processes of technologically relevant organic and hybrid materials such as polymers, COFs, MOFs, and perovskites are mainly governed by the quantum mechanical behavior of mobile quasiparticles, such as Frenkel, charge-transfer, and Wannier–Mott excitons, polarons and bipolarons, trions, and the interaction of mobile quasiparticles with intra- and inter-molecular vibrational modes.^{129–144} These vibronic effects, which arise from the coupling of the electronic transitions with the nuclear vibrational motion, play a central role in determining the photophysical response of organic^{145–147} and hybrid materials^{148–154} as well as influence the excited state dynamics in chemical and biological systems.^{155–163} It is therefore not surprising that any progress in the design of novel materials warrants a robust theoretical methodology that can provide an in-depth understanding of how the complicated interplay between photons, excitons, polarons, bipolarons, phonons, and spins influences the photoinduced excited state processes of a broad range of semiconducting materials.

Despite significant recent progress, two main challenges still persist which involve a quantitative understanding of how electron–phonon coupling and defects influence the electronic, optical, and transport properties of functional electronic materials. Although, excited state properties of materials can be modeled using linear-response time-dependent density functional theory (LR-TDDFT) or the Bethe–Salpeter equation (BSE),¹⁶⁴ the presence of a large number of atoms in 2D materials makes the application of LR-TDDFT and BSE computationally very demanding (however, recent advances do look very promising^{165,166}). Moreover, electron–phonon coupling and different forms of electronic and conformational defects play fundamental roles in determining the photophysical response and, consequently, the transport properties of most organic and hybrid materials. Although, LR-TDDFT/BSE approaches have been successfully employed to investigate the photophysical response of MOFs,^{167–171} COFs,^{141,172–174} and perovskites,^{130,142,175–182} to the best of our knowledge, none of the existing methodologies simultaneously take into account aggregation, electronic coupling, strong electron–phonon coupling, and crystalline disorder on equal footing.

An exact treatment of electron–phonon coupling is a pressing challenge since the Hilbert space for most quantum systems grows exponentially with increasing system size and



number of molecules. Overcoming this computational complexity involves the inevitable approximation of sacrificing the quantum description of the nuclei, which reduces to treating the nuclear motion adiabatically by employing the Born–Oppenheimer approximation (BOA). First-principles calculations based on the BOA such as finite differences and density functional perturbation theory have been used to interpret optical properties, charge transport, and defects in semiconductors.¹⁸³ However, this perspective highlights photophysical processes in which the nuclear vibrational kinetic energies are not negligible and undergo rapid nuclear reorganization, which therefore necessitates the explicit inclusion of nuclear quantum effects and, consequently, invalidates the BOA. In this regard, it should be noted that excellent non-adiabatic approaches, including mixed quantum-classical descriptions, have been successfully employed to investigate the photophysical processes and excited state dynamics of various systems.^{184–189}

Coarse-graining is another efficient strategy to quantitatively describe electron–phonon coupling in large, non-rigid “vibronic” systems. Since the pioneering work by Drude,^{190,191} Sommerfield,¹⁹² Hubbard,¹⁹³ Heisenberg,¹⁹⁴ Holstein^{195,196} among others, coarse-grained tight-binding model Hamiltonians have been successfully employed to investigate the electronic, optical, and transport properties of semiconducting materials.^{104–106,197–201} The major approximation typically employed in tight-binding modeling involves simplifying the complicated many-body electronic system to an one-electron or single orbital model. In Holstein-based approaches, another major simplification is the harmonic oscillator approximation which considers the nuclear displacements as coupled quantum harmonic oscillators. Such simplifications are however not sufficient for practical applications, since the exact diagonalization becomes computationally intractable for large “vibronic” systems, which is the focus of this perspective. For example, the Holstein model can be exactly solved only for a few sites. Besides various approaches proposed in the literature to address this problem, including hierarchical equations of motion,^{202–205} one potential solution is to specifically choose an accurate basis set for the diagonalization of the Holstein Hamiltonian. In this context, the multiparticle basis set, pioneered by Philpott,²⁰⁶ developed and glorified by Spano,^{146,147,207–209} and employed by others^{210–215} has proved to be an excellent choice for diagonalizing the Holstein Hamiltonian. Multiparticle modeling of the Holstein Hamiltonian quickly becomes computationally expensive with increasing dimensions of the material unit cell, which is particularly relevant in the case of porous frameworks such as COFs and MOFs. In this context, taking advantage of sparse matrix techniques and MPI parallelization on multinode clusters, we have shown that it is possible to extend the application of multiparticle modeling to large “vibronic” 3D systems, with negligible loss of accuracy.^{216,217}

The article is organized as follows: in Section 2 we briefly discuss the MHF. Section 3 highlights the photophysical signatures of Frenkel, charge-transfer, and Wannier–Mott excitons in organic (polymers and COFs) and hybrid (MOFs and

perovskites) materials. The role of “excitonic polarons”, *i.e.*, excitons dressed with intramolecular vibrations is also discussed. Special emphasis is placed on understanding how several factors, such as the nature of aggregation, packing arrangement, particle size, relative humidity, and defects determine the UV-vis to near-IR spectral response of donor–acceptor (D–A) COFs. The exciton fine structure observed in layered perovskites, which is a topic of considerable speculation,^{152,218–220} is also discussed. Section 4 focuses on the importance of mid-IR photophysical response of polarons and the correlations between mid-IR signatures and polaron coherence lengths. The similarity in the spectral response of polarons in polymers, COFs, MOFs, and perovskites is highlighted, and relevant factors affecting charge transport are reviewed. It is a daunting task to provide a comprehensive review that includes all relevant references on photophysical processes observed in organic and hybrid materials and this perspective only focuses on select photophysical signatures that are intriguing from the point of view of the MHF. Although previous reviews and perspectives have separately focused on optoelectronic processes in organic and hybrid materials,^{144,221–226} to the best of our knowledge, no prior studies have attempted to provide an interpretation of the photophysical signatures of both organic and hybrid organic–inorganic materials using a common theoretical platform – the Multiparticle Holstein Formalism.

2 Theoretical framework

The Multiparticle Holstein Formalism (MHF) is based on coarse-grained Holstein-style Hamiltonians in which electronic coupling, electron–phonon coupling, electrostatic interactions, and different forms of long- and short-range defects are treated on “equal footing” without invoking the BOA. The key advantage of the MHF is the nonadiabatic treatment of the electron–phonon coupling which allows for a fully quantum-mechanical treatment of both the kinetic and potential energies of the nuclei, thus bypassing the conventional BOA. The creation of neutral excitations (*e.g.*, excitons) or charged excitations (*e.g.*, polarons) in conjugated organic molecules, which are active components in MOFs, COFs, and oligothiophene based perovskites, is accompanied by significant nuclear relaxation, the bulk of which occurs along the aromatic to quinoidal stretching vibrational mode having a frequency that lies in the range between 0.15 eV and 0.18 eV.^{147,207,227} This local nuclear relaxation energy plays a central role in the photophysical and transport properties, examples of which will be discussed in the context of COFs, MOFs, and 2D perovskites later in the perspective. What truly distinguishes our approach is an essentially exact (albeit numerical) treatment of the Holstein Hamiltonian using a multiparticle basis set²⁰⁶ to obtain accurate eigenstates and energies important for the construction of absorption (and PL) lineshapes. The Hamiltonian can be modified to include different forms of electronic and structural defects which are ubiquitous in light absorbing semiconducting materials. The MHF has been very successful in accounting for the spectral properties of molecular aggregates and



crystals,^{145,147,207,210,211,227,228} conjugated polymers,^{229–241} COFs,^{216,217} and layered perovskites²⁴² in the mid-infrared (mid-IR) and UV-vis spectral regions.

2.1 Frenkel exciton

In the subspace containing a local Frenkel excitation (see Fig. 1a), where the n th repeat unit in the lattice denoted by $|n\rangle$ hosts an electron-hole pair (*i.e.*, a Frenkel exciton), the Hamiltonian (with $\hbar = 1$) can be divided into electronic and vibronic contributions,

$$H_{\text{FE}} = H_{\text{FE-el}} + H_{\text{FE-vib}} \quad (1)$$

with the purely electronic part of the Hamiltonian given by

$$H_{\text{FE-el}} = \omega_{0-0} \sum_n |n\rangle\langle n| + \sum_{m,n} J_{m,n} \{ |m\rangle\langle n| + |n\rangle\langle m| \} \quad (2)$$

and the vibrational energies and vibronic coupling are given by

$$H_{\text{FE-vib}} = \omega_{\text{vib}} \sum_n b_n^\dagger b_n + \lambda \omega_{\text{vib}} \sum_n (b_n^\dagger + b_n + \lambda) |n\rangle\langle n| \quad (3)$$

In eqn (2), the first term represents the energy of the Frenkel exciton. Exciton transport between neighboring sites $|n\rangle$ and $|m\rangle$ is governed by long-range intermolecular Coulomb coupling as well as a short-range superexchange contribution which mainly arises due to wavefunction overlap between the adjacent chromophores. The coupling values are generally derived from atomic transition charge densities and can be calculated using TDDFT methods.^{243–246} Upon electronic excitation, Frenkel excitons in π -conjugated organic molecules couple very strongly to the aromatic to quinoidal vibrational mode, ω_{vib} , with frequency in the range between 1200 and 1500 cm^{-1} . The two terms in eqn (3) account for the vibronic coupling where the operators create (annihilate) a vibrational quantum of energy on the n th unit in the ground state (S_0) of the corresponding

potential energy well. The strength of the electron-phonon coupling is governed by the Huang-Rhys (HR) factor, λ^2 , and the nuclear relaxation energy upon vertical Franck-Condon excitation is given by $\lambda^2 \omega_{\text{vib}}$. λ^2 is a dimensionless quantity that determines the relative displacement of the minima of the ground and excited potential well along the intramolecular vibrational coordinate (Fig. 1b). In the case of excitons in conjugated polymers, the value of λ^2 generally lies between 1 and 2.²⁴⁰

2.2 Charge-transfer exciton

In closely packed structures, such as polymers, COFs, and MOFs, where the inter-chain/inter-framework π -stacking distances lie in the range between 0.30 nm and 0.40 nm, there exists significant π -orbital overlap between the HOMO and LUMO of neighboring π -conjugated units. In such circumstances, local Frenkel excitations dissociate into charge-transfer states, with the electrons and the holes residing on neighboring units, as shown schematically in Fig. 1a. As a consequence, considering only long-range intermolecular Coulomb coupling is not sufficient to accurately describe the underlying physics of the system, and short-range superexchange contributions arising from wavefunction overlap need to be considered. To account for the role of intermolecular charge-transfer, the Frenkel-Holstein Hamiltonian described in eqn (1) can be extended and the total Hamiltonian is given by

$$H_{\text{total}} = H_{\text{FE}} + H_{\text{CT}} \quad (4)$$

where H_{FE} is given in eqn (1) and the appropriate vibronically-coupled charge-transfer Hamiltonian (with $\hbar = 1$) can be divided into electronic and vibronic contributions,

$$H_{\text{CT}} = H_{\text{CT-el}} + H_{\text{CT-vib}} \quad (5)$$

with the purely electronic part given by



Fig. 1 (a) Simplified view of various forms of neutral and charged excitations. (b) Nuclear potential well corresponding to the aromatic to quinoidal stretching mode, Q , in the ground and excited electronic states for each isolated molecular unit. ω_{vib} refers to the vibrational energy and the nuclear relaxation energy is denoted by $\lambda^2 \omega_{\text{vib}}$. (c) Schematic showing one-particle states, *i.e.*, vibronic excitations (top panel) and two-particle states, *i.e.*, vibronic/vibrational exciton pair.



$$\begin{aligned}
 H_{\text{CT-el}} = & \sum_n \sum_{s=-1,1} \left\{ t_{n,n+s}^e |n\rangle \langle n, n+s| + \text{h.c.} \right\} \\
 & + \sum_n \sum_{s=-1,1} \left\{ t_{n,n+s}^h |n\rangle \langle n+s, n| + \text{h.c.} \right\} \\
 & + \sum_n \sum_{s=-1,1} E_{n,n+s}^{\text{CT}} |n, n+s\rangle \langle n, n+s|
 \end{aligned} \quad (6)$$

and the vibrational contribution given by

$$\begin{aligned}
 H_{\text{CT-vib}} = & \omega_{\text{vib}} \sum_{n,s=-1,1} \left\{ \lambda_+ (b_n^+ + b_n + \lambda_+) \right. \\
 & \left. + \lambda_- (b_{n+s}^- + b_{n+s} + \lambda_-) \right\} |n, n+s\rangle \langle n, n+s| \quad (7)
 \end{aligned}$$

where the charge-transfer excitations are limited to nearest neighbors. The charge-separated state is denoted by $|n, n+s\rangle$, with sites $|n\rangle$ and $|n+s\rangle$ hosting a cation and an anion, respectively. In eqn (6), the first two terms account for nearest-neighbor hopping of the electron and the hole, respectively, and E_{CT} determines the energy of the charge-separated state. In addition to the ground-state nuclear potential, there exist three excited-state nuclear potentials corresponding to the fragment's electronic states representing a Frenkel-like excitation, a cation, and an anion, respectively. As shown in Fig. 1b, all potentials are assumed to have identical curvature but are generally shifted relative to the ground state potential based on the value of HR factors. For Frenkel-like excitations, the HR factor is defined as λ^2 , while the HR factors for the cations and anions are λ_+^2 and λ_-^2 , respectively, as shown in eqn (7). $\lambda_+^2 \omega_{\text{vib}}$ and $\lambda_-^2 \omega_{\text{vib}}$ determine the cationic and anionic nuclear relaxation energies respectively. Both vibronic coupling and charge-transfer mediated interactions strongly influence the photophysical and transport properties of the organic molecules, which are the primary building blocks of COFs and are also active components in organic-inorganic hybrid materials.

2.3 Polaron

Analogous to the case in Frenkel excitons, eqn (1) can also be efficiently used to describe polarons. Unlike in the case of excitons, where the n th unit in eqn (2) denotes an electron-hole pair, the n th unit for polarons in eqn (2) indicates a charge as shown in Fig. 1a. In addition, differently from excitons, in the case of polarons, charge transport between sites $|n\rangle$ and $|m\rangle$ is primarily governed by the charge resonance integral, $t_{m,n}$, which can be evaluated by electronic structure methods.^{247,248} Finally, while the exciton model retains the local HOMO and LUMO for each site $|n\rangle$, only the local HOMO for each repeat unit, $|n\rangle$, is retained in the case of polarons, as shown in Fig. 1a. For both excitons and polarons, the first term in eqn (2) determines the energy of the excited state of the isolated unit which hosts the exciton/polaron relative to the ground state which contains no excitons or polarons. In the case of excitons, ω_{0-0} in eqn (2) refers to the adiabatic energy required to create an electron-hole pair, while in the case of polarons, ω_{0-0} refers to the ionization energy required to create the hole. However, just like in the exciton model, creation of polarons is also accompanied by significant nuclear relaxation along the dominant aromatic-quinoidal stretching coordinate.

The value of λ^2 in the case of polarons is approximately half of the exciton value.²⁴⁹

2.4 Multiparticle basis set

The main computational challenge is to obtain accurate eigenstates of the Holstein-based Hamiltonians in light of an essentially infinite basis set arising from an unlimited number of allowed vibrations. The “trick” is to zero in on the sub-basis which accurately represents the optically allowed states and build in additional basis functions in a systematic manner. To this end, we can employ a multiparticle basis set, in which the basis set can be truncated to include all one-, two-, ..., s -particle states.²⁰⁶ In the multiparticle approach, each basis function contains information about the location of the vibronically excited chromophore as well as additional purely vibrationally excited molecules.

A single-particle basis state which can either be a single hole or a single exciton (Fig. 1a), is denoted as $|n, \tilde{\nu}\rangle$ to indicate that the hole or the exciton resides on the n th unit with a $\tilde{\nu}$ vibrational quanta in the shifted (S_+) potential well (Fig. 1c). All the remaining units are in their vibrationless ground states, which implies that the units have filled HOMOs with no vibrations in the S_0 well. In a two-particle basis state, denoted as $|n, \tilde{\nu}; n', \tilde{\nu}'\rangle$, the n th unit is ionized with $\tilde{\nu}$ vibrational quanta in the S_+ potential well, while the unit at n' is electronically neutral, with $\tilde{\nu}' > 0$ vibrational quanta in the unshifted S_0 potential well. All the remaining units are in their vibrationless ground states. Three, four, and higher particle states with three or more monomer excitations (electronic plus vibrational) can also be included. As expected, the basis set grows exponentially with increasing number of units. Fortunately, for most practical applications, accurate solutions of the Holstein-style Hamiltonians can be obtained by truncating the multiparticle basis set to contain only one and two particle states. The total number of vibrations, ν_{max} , is capped to a maximum of 4 which is sufficient to obtain converged absorption and emission spectra.^{227,250}

Within the two particle approximation, the eigenstates of the Hamiltonian in eqn (4) can be expanded in the local multiparticle basis set composed of both Frenkel and CT multiparticle states basis as

$$\begin{aligned}
 |\Psi_\alpha\rangle = & \sum_n \sum_{\tilde{\nu}=0,1,\dots} c_{n,\tilde{\nu}}^\alpha |n, \tilde{\nu}\rangle + \sum_{n,\tilde{\nu}=0,1,\dots} \sum_{n',\tilde{\nu}'=1,2,\dots} c_{n,\tilde{\nu};n',\tilde{\nu}'}^\alpha |n, \tilde{\nu}; n', \tilde{\nu}'\rangle \\
 & + \sum_n \sum_{\tilde{\nu}^+=0,1,\dots} \sum_{s=\pm 1, \pm 2, \dots} \sum_{\tilde{\nu}^-=0,1,\dots} d_{n,\tilde{\nu}^+;s,\tilde{\nu}^-}^\alpha |n, \tilde{\nu}^+; n+s, \tilde{\nu}^-\rangle
 \end{aligned} \quad (8)$$

where the first two terms in eqn (8) represent one and two particle Frenkel excitons. The last term in eqn (8), $|n, \tilde{\nu}^+; n+s, \tilde{\nu}^-\rangle$, denotes two particle charge separated state in which site $|n\rangle$ which hosts a cation has $\tilde{\nu}^+$ vibrational quanta in the shifted, excited potential well while site $|n+s\rangle$ which hosts an anion has $\tilde{\nu}^-$ vibrational quanta in the shifted excited potential well.

The multiparticle basis set can be similarly extended to describe correlated multiple excitations such as bipolarons,²⁵¹ biexcitons, trions, tripolarons, which are currently under



investigation. It should be noted that the multiparticle basis set is not a convenient basis set in the regime of strong electronic coupling since it requires the inclusion of higher particle states. In such scenarios, the exciton-phonon basis set, which has been successfully employed in earlier studies,^{213,252–254} is a more appropriate basis set.

2.5 Defects

Inhomogeneous polarizing environments such as structural and lattice imperfections, that is ubiquitous in most organic and hybrid materials, can localize quasiparticles (*i.e.*, electrons and holes) in deep traps. Different forms of common inhomogeneities in materials can arise from variations in nearest-neighbor π -stacking distances and torsional angles within the functional groups of the molecular building blocks. Static defects in materials can be efficiently described by considering random distribution of Gaussian site energy fluctuations having a standard deviation σ .²⁵⁵ The presence of defects in most materials have a profound effect on the spectral signatures and charge transport properties of organic and hybrid materials, and can be accounted phenomenologically by incorporating diagonal and off-diagonal disorder in the model. The effective Hamiltonian describing defects can be written as

$$H_{\text{defects}} = \sum_n \Delta_n |n\rangle\langle n| + \sum_{m,n} \Delta J_{m,n} (|m\rangle\langle n| + |n\rangle\langle m|) \quad (9)$$

where Δ_n is obtained by selecting the energy fluctuations from a Gaussian distribution with standard deviation σ

$$p(\Delta_n) = \frac{1}{\sqrt{2\pi}} \sigma \exp\left(-\frac{\Delta_n^2}{2\sigma^2}\right) \quad (10)$$

Similarly, $\Delta J_{m,n}$ refers to random deviations in the electronic couplings which arise due to random changes in the separation between neighboring units. As detailed in ref. 229 and 250, the degree of disorder can be spatially correlated with the two extreme limits being long-range (*i.e.*, infinite spatial correlation) and short-range (*i.e.*, no spatial correlation). In the limit of short-range disorder, for every disorder configuration, every unit in the lattice is assigned a random energy from a Gaussian distribution having standard deviation σ (eqn (10)). In the opposite extreme of long-range disorder, within each disorder configuration, all the units in the lattice are assigned identical energy detunings. Knapp have further shown that the long- and short-range disorder can be distinguished by tuning the spatial correlation length.²⁵⁶

2.6 Absorption

Since the discussion in Sections 3 and 4 is focused on excitonic and polaronic photophysical signatures in organic and hybrid materials, we briefly discuss the absorption in the far to mid-IR and UV-vis spectral region. For both Frenkel excitons (FE), and polarons (p), the absorption spectrum corresponding to an ensemble of disordered lattice sites is generally expressed as

$$A_{\text{FE}(P)}(\omega) \equiv \left\langle \sum_i f_i^{\text{FE}(P)} W_{\text{LS}} [\hbar\omega - (E_i - E_G^{\text{FE}(P)})] \right\rangle_C \quad (11)$$

where the bracket $\langle \dots \rangle_C$ represents an average over an ensemble of disorder configurations, and the oscillator strength, $f_i^{\text{FE}(P)}$, is given by

$$f_i^{\text{FE}(P)} = (E_i - E_G^{\text{FE}(P)}) |\langle \psi_i | \hat{M}_{\text{FE}(P)} | G_{\text{FE}(P)} \rangle|^2 \quad (12)$$

here, $|G_{\text{FE}(P)}\rangle$ is the ground-state wavefunction of both polarons and excitons with energy $E_G^{\text{FE}(P)}$, and the sum extends over all one-exciton or one-polaron eigenstates, $|\psi_i\rangle$, with energies, E_i , found through the diagonalization of the total Hamiltonian in eqn (1). In the case of Frenkel excitons, the transition is from a ground state which contains no excitons to a state which contains single excitons. In the case of polarons, the transition instead takes place from a ground state, which already contains a hole, to an excited state which contains a hole. Therefore, the ground state in the case of a polaron is the lowest eigenstate of the Hamiltonian in eqn (1). Hence, Frenkel excitons absorb in the UV-vis, while polarons absorb in the mid-IR spectral region. For a more elaborate discussion regarding the optical properties of excitons and polarons within the MHF, we refer readers to ref. 250.

3 Photophysics of excitons

3.1 Excitons in COFs

Several research groups have successfully employed the strategy of aligning donor (D) and acceptor (A) building blocks in order to modulate the optical, electronic, and transport properties of various COF structures. Since providing a comprehensive review of the optical properties of D-A COFs is not the goal of this section, we only focus on selected photophysical signatures in the UV-vis energy region and emphasize direct correlations between the spectral features and potential applications including photothermal activity, electrochromism, light harvesting, framework stability, nature of aggregation, and energy and charge transport. Within this context, an important research question can be raised: is it possible to unravel the complex interplay among electronic coupling, vibronic coupling, electrostatic interactions, and different forms of defects through the interpretation of well defined spectral signatures? More specifically, can distinct spectral signatures be identified that can be used as efficient screening protocols for synthesizing new COF-based structures for desired applications?

Effect of aggregation. Distinct optical signatures for H- and J-aggregation, based on the Frenkel exciton theory,^{259,260} which involves the point dipole approximation of Coulomb coupling, was first introduced by Kasha.^{261–265} In the case of H-aggregation, where the transition dipole moments between the adjacent chromophores maintain a “side-by-side” arrangement, positive Coulomb coupling results in a blue shift of the main absorption peak compared to the absorption of the monomeric unit. In J-aggregates, the dipoles in the adjacent chromophores maintain a “head-to-tail” arrangement that



leads to negative Coulomb coupling and a red shift of the main absorption band compared to the monomer.^{261,263}

While 2D COFs are usually described as eclipsed layered structures, experimental and computational studies have provided convincing evidence that the layers are slightly offset from one another.^{266–273} Moreover, relatively broad peaks in the powder X-ray diffraction patterns do not rule out the possibility of small offsets in the inter-layer stacking arrangement.²⁷⁴ Within this context, highly crystalline solid-state J-aggregate imine-linked COFs, which not only enable prolonged lifetime of singlet excitons but also facilitate exciton delocalization and stabilization of the excited species, have been synthesized by the Bein group.²⁷⁵ The incorporation of porphyrin and thienothiophene units as molecular building blocks result in the formation of J-aggregate stacks having unprecedented COF domain sizes (up to 100 nm). H-aggregate COFs exhibiting high charge mobility have also been reported.²⁵⁷

Apart from the usual Kasha signatures predicting aggregation-induced spectral shifts between coulombically coupled chromophores, additional vibronic signatures to differentiate between H- and J-aggregates were introduced by Spano.¹⁴⁶ More specifically, it was shown that the ratio of the first two vibronic peaks referred to as A_1 (0–0) and A_2 (0–1) decreases with increasing exciton bandwidth for H-aggregates but increases for J-aggregates.¹⁴⁶ While long-range intermolecular Coulomb coupling predicts aggregation-induced blue and red shifts for H- and J-aggregates, respectively, such a scheme breaks down in closely π -stacked systems, due to significant wavefunction overlap and the emergence of short-range intermolecular charge transfer (ICT) between the neighboring chromophores.^{145,227} In such scenarios, assigning the type of aggregation based on spectral shifts may be misleading, and the nature of aggregation can be reliably predicted from the evolution of the vibronic signatures in the UV-vis absorption and emission lineshapes. Theoretical simulations based on the Hamiltonian shown in eqn (4) that explicitly includes short-range ICT have showed that the interference between long-range Coulomb coupling and short-range superexchange contributions result in a rich array of possible aggregate types (HH, HJ, JH, and JJ type aggregates) with contrasting photophysical signatures and transport properties.¹⁴⁵ HJ type aggregates in particular has been extensively investigated in the case of conjugated polymer films and molecular aggregates.^{276–284}

The experimental realization of H- and J-type aggregation have been observed in COF-5 that exhibits large exciton diffusion lengths.¹⁴⁰ While a red shift was observed in the absorption spectrum of COF-5, which indicates J-type aggregation, the change in vibronic ratios in the emission spectrum suggested a H-type coupling.¹⁴⁰ H and J aggregation have also been reported in TAT COF, which was described as non-fluorescent J-type class of aggregates.¹⁴¹

Coexistence of H and J aggregation in COFs have been previously observed in literature, but have not been discussed in detail to date. For example, perfectly stacked COF structures were synthesized by the Jiang group by combining phthalocyanine units with benzene diboronic acid.²⁵⁷ Owing to the well-ordered arrangement of the π -stacked phthalocyanine units,

NiPc COF exhibits enhanced light-harvesting capability in the visible and near-IR spectral regions, which facilitates efficient charge carrier transport. Although referred to as H-aggregate, the UV-vis absorption spectrum of NiPc COF displays J-type vibronic signatures. In particular, the absorption band (“B” band) of NiPc COF (Fig. 2a) at 380 nm is blue-shifted by 32 nm compared to the monomer precursor $[(\text{MeO})_8\text{PcNi}]$. Although this blue shift indicates the formation of phthalocyanine H-aggregates within the stacked COF structure, the Q bands of the NiPc COF, which are observed at 635 and 686 nm, are red-shifted by 12 nm from those of the $[(\text{MeO})_8\text{PcNi}]$ monomer. More importantly, the ratio of the intensities of the 0–0 and 0–1 vibronic peaks is larger in the case of the NiPc COF compared to the monomer (Fig. 2a), which is a well defined signature of J-type aggregation.²⁸⁵

In ref. 258, the Jiang group used electron-donating metallophthalocyanines and electron-accepting diimide derivatives as building blocks for the synthesis of D–A COFs (Fig. 2b), resulting in the formation of “super-heterojunctions” that display long-lived charge separation and exhibit remarkable photochemical properties. Compared to the phthalocyanine monomeric units, the UV-vis absorption measurements of the COF structures ($\text{D}_{\text{CuPc}}\text{-A}_{\text{PyrDI}}$) displayed blue-shifted B bands, indicating H-aggregation. On the other hand, a red shift was observed in the low energy absorption bands of the COF structures compared to the imide building blocks, indicating J-aggregation (Fig. 2c). From the experimental observations, it was concluded that the COF structure is able to merge the absorption of the separate building blocks, which results in a broader absorption profile. However, in-depth theoretical investigations may provide deeper insights since perylene diimide (PDI) aggregates alone display two asymmetrically broadened absorption bands on transformation from one aggregate form to the other, with one band being red shifted and the other being blue shifted relative to the absorption of the monomeric unit.^{228,286–291}

In this context, the steady state absorption and emission spectra of two PDI derivatives were theoretically investigated using the Frenkel–CT/Holstein Hamiltonian in ref. 243. The Frenkel–CT/Holstein Hamiltonian shown in eqn (4) was able to reproduce the salient spectroscopic signatures of both the PDI derivatives. The authors concluded that the band splitting observed in PDI aggregates primarily arises due to the coupling between Frenkel and charge-transfer excitons in the resonant regime, which is driven by intermolecular electron and hole transfer. Theoretical investigations based on the MHF in ref. 243 also shed light on how the vibronic spectral features of the two main bands in the UV-vis absorption of PDI aggregates are governed by the interplay between long-range Coulomb coupling and short-range superexchange CT-mediated couplings. Hence, to obtain a detailed understanding of the factors that govern the photophysical response of COFs, it is important to simplify the problem by reducing the frameworks into their isolated monomeric components, which would allow for a systematic analysis of the evolution of the UV-vis spectral signatures from the isolated monomeric units to the aggregated monomers and 3D frameworks.



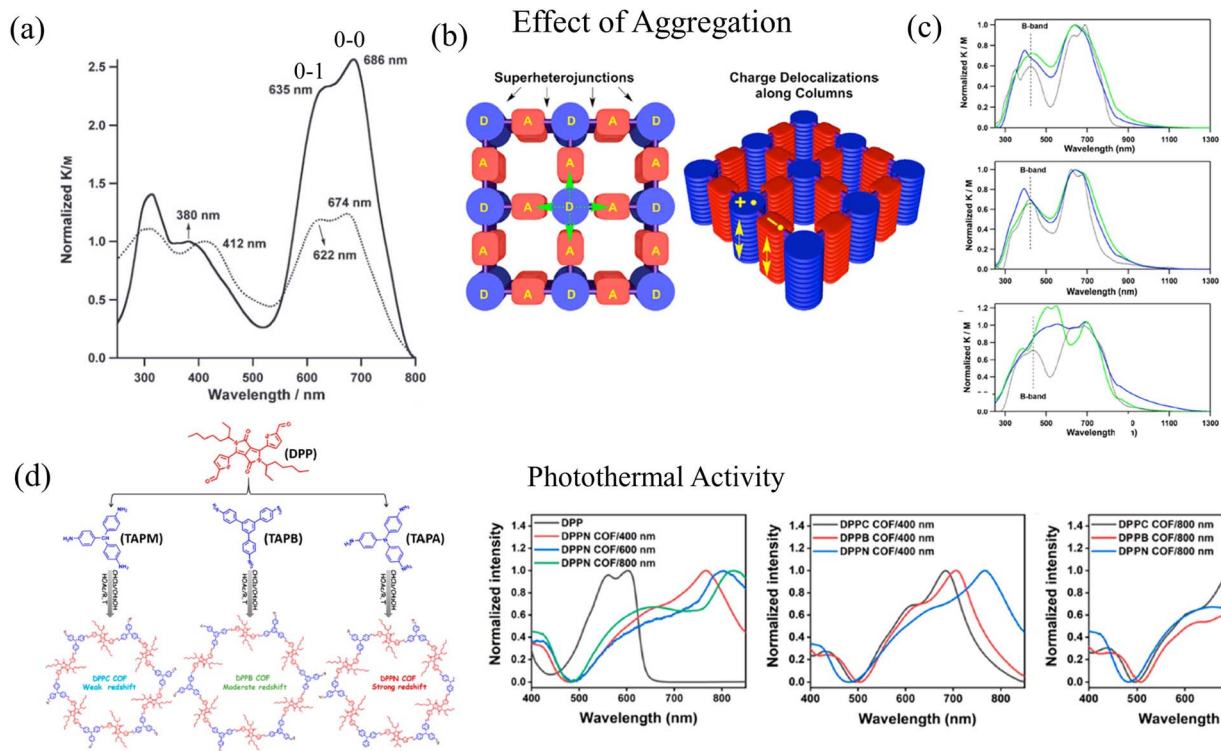


Fig. 2 (a) H- and J-type bands observed in UV-vis absorption of NiPc COF (solid black). Although referred to as H-aggregates, the ratio of the intensities of the vibronic peaks I_{0-0}/I_{0-1} is greater in NiPc COF compared to the (MeO)₈PcNi monomer (dotted black) suggesting J-type aggregation.²⁵⁷ Copyright 2011 John Wiley & Sons, Inc. (b) Schematic of segregated bicontinuous π -columnar arrays observed in COFs.²⁵⁸ (c) UV-vis observation observed in D_{MPC}-A_{DI} COFs also display H- and J-type signatures in the UV-vis.²⁵⁸ (d) UV-vis absorption of DPP-based donor-acceptor COFs directly correlates with the COF particle size.⁴⁷ (b) and (c) Reprinted with permission from ref. 258. Copyright 2015 American Chemical Society. (d) Reprinted with permission from ref. 47. Copyright 2021 American Chemical Society.

Effect of COF particle size. In a recent study, Schiff-based reactions were used to synthesize a series of size-controllable nanoscale COFs (DPPC, DPPN, DPPB) with uniform and spherical morphology.⁴⁷ This was achieved by incorporating D-A building blocks based on diketopyrrolopyrrole (DPP) units, which resulted in a broad absorption profile that extended into the near-IR (Fig. 2d). Additionally, the UV-vis spectral response showed a positive correlation with COF particle size, and the maximum of the absorption spectrum red-shifted from 768 to 824 nm with increase in particle size from 400 nm to 800 nm. Interestingly, besides the observed red shift relative to the DPP building block, the spectral lineshapes of the corresponding COFs dramatically differ with increasing particle size and display the emergence of a featureless broad peak centered around 600 nm (Fig. 2d).

Effect of electrochromism. Electrochromism is a property that describes reversible color changes of a material in response to an externally applied electric current. The Bein group paired electron deficient isoindigo-based building blocks with electron-rich pyrene motifs to synthesize highly crystalline imine linked D-A COFs that absorb light throughout the visible and near-IR energy range.²⁹³ The absorption spectrum of the COF films displays a dominant near-IR band followed by a lower-intensity UV-vis band at a higher energy. A red shift in the absorption spectrum was observed depending on the choice

of the molecular building blocks.²⁹³ In a follow-up study using similar D-A-D motifs and incorporating modified thienoisindigo building blocks, Bessinger *et al.* synthesized a series of highly efficient, fast-switching, and stable electrochromic 2D COFs (Fig. 3a).²⁹² Positive correlations of the UV-vis and near-IR spectral response with electrochromic properties were reported. The electrochemical oxidation of py-ttTII COF was associated with the bleaching of the main absorption band in the neutral COF structure which was accompanied by the simultaneous emergence of new spectral features in the near-IR energy range (Fig. 3b). The first and second oxidation steps produced spectral features at 1000 and 900 nm which were attributed to the formation of polarons and bipolarons, respectively. These results indicate the need to identify spectral signatures that can be efficiently used to differentiate polarons, bipolarons, and excitons in neutral and oxidized COF structures.

Effect of relative humidity. Li *et al.* reported a strategy for engineering the bandgap of 2D COFs by introducing D-A units into the COF framework.²⁹⁴ Triphenylamine and salicylideneaniline building units were used to synthesize 2D COFs that exhibit eclipsed stacking arrangement and excellent nonlinear optical limiting behavior. It was also found that the UV-vis spectral signatures of the COF structures were sensitive to the adsorption of moisture. In order to monitor the correlations between the spectral response and band-gap narrowing, the UV-





Fig. 3 (a) Example of electrochromic COFs synthesized by the Bein group.²⁹² UV-vis spectral features of D–A COFs as a function of (b) oxidation,²⁹² (c) monomer building blocks,²⁹³ (d) relative humidity,²⁹⁴ and (e) metal centers.²⁹⁵ (f) UV-vis absorption spectrum of highly emissive D–A COFs.¹⁴¹ (a) and (b) Reprinted with permission from ref. 292. Copyright 2021 American Chemical Society. (c) Reprinted with permission from ref. 293. Copyright 2017 American Chemical Society. (d) Reprinted with permission from ref. 294. Copyright 2018 American Chemical Society. (e) Reprinted with permission from ref. 295. Copyright 2019 American Chemical Society. (f) Reprinted with permission from ref. 141. Copyright 2021 American Chemical Society.

vis measurements were performed as a function of relative humidity. While the absorption spectrum for dry or fully wetted TF-TAPA COF remained unchanged with increasing relative humidity, the absorption spectrum for Sa-TAPA further red-shifted to the near-IR, with distinct color change from red to black (Fig. 3d). This red-shift was attributed to conformational changes in the framework which was further confirmed by FT-IR and NMR studies. The observed sensitivity of the UV-vis spectral signatures to the uptake of moisture and stability of the COF structure emphasizes the importance of investigating the role of structural and conformational disorder on the photophysical response of COFs as well as how disorder affects the electronic properties of COFs.

Effect of metal center. In order to investigate the effect of metal centers, two structurally and morphologically similar π -conjugated 2D COFs based on Zn- and Cu-phthalocyanine macrocycles and pyrazine linkers were synthesized by Wang *et al.*²⁹⁵ Although the incorporation of different metal centers results in distinct spectral signatures in the UV-vis as shown in Fig. 3e, it was demonstrated that changing the metal center from Zn to Cu in the phthalocyanine moiety has negligible impact on the charge carrier transport properties, with the hole mobility being negligible along the COF plane and finite between the COF planes.

Light harvesting COFs. Two highly emissive, fully conjugated D–A sp^2 -C-COFs were recently synthesized by Yang *et al.* who showed that the exciton relaxation pathway and photoluminescence quantum yield were controlled by planarity, conjugation, and interlayer aggregation.¹⁴¹ Using a combination

of experimental and TDDFT calculations, direct correlations were established between the COF structure and associated light harvesting properties, charge transfer, emission quantum efficiency, and photophysical signatures (Fig. 3f). In particular, it was emphasized that in order to have a better understanding of excitonic effects in COF structures, it is crucial to consider the contributions from superexchange ICT coupling as discussed earlier in this section.

Application of the MHF. As shown in Fig. 4, the characteristic UV-vis spectral response for most D–A COFs involves the presence of a lower energy band (B band), typically starting at 500 nm and extending into the near-IR energy range, accompanied by a higher energy band (Q band) between 300 nm to 500 nm. We employ the Hamiltonian in eqn (4) to accurately reproduce the UV-vis absorption spectrum of py-ptII COF reported in ref. 293 (Fig. 4). In an earlier study, Qarai *et al.* used the Frenkel–CT Holstein Hamiltonian (eqn (4)) to account for the steady state UV-vis absorption spectrum of push–pull low band gap PffBT4T copolymer.²⁸⁵ As for PffBT4T copolymer, the unpolarized UV-vis absorption spectrum for py-ptII COF was obtained using eqn (11) and the multiparticle basis set in eqn (8) was used to describe the Hamiltonian in eqn (4).

Analogous to the case in 1D copolymers,²⁸⁵ good agreement between the measured and simulated absorption spectrum of py-ptII COF was obtained using a single chain having a donor–acceptor–donor (DAD) alternate sequence of coupled chromophores. A comparison between the experimental absorption spectra of py-ptII COF and PffBT4T copolymer²⁸⁵ reveals that the spectral features in both py-ptII COF and PffBT4T copolymer are



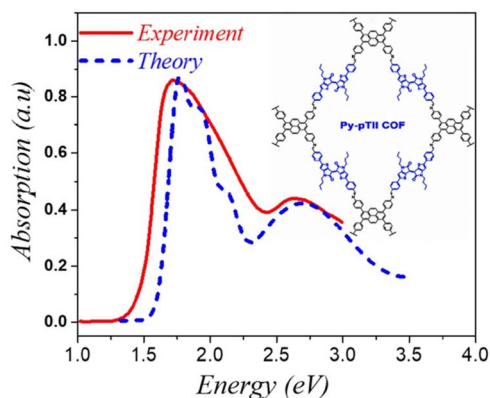


Fig. 4 Comparison of the simulated spectrum using the MHF with the measured absorption spectrum of py-ptII COF replotted from ref. 293.

quite similar. However, unlike in the case of PffBT4T, the absorption spectrum of the py-ptII COF does not display the pronounced vibronic structure in the low-energy Q band. The vibronic features in py-ptII COF are most likely obscured due to the presence of inherent electronic and structural defects.

The close similarity between the absorption spectra of py-ptII COF and PffBT4T copolymer also suggests that inter-framework interactions may be of secondary importance in the case of py-ptII COF. However, some caution should be used before generalizing this conclusion to all D–A COFs since other factors might determine the optical properties of COFs. For example, the physical mechanisms responsible for the emergence of a featureless peak centered at ~ 630 nm (Fig. 2d), which broadens with increasing COF particle size or increasing electron donating ability of the monomer units in DPP-based COFs,⁴⁷ are not well understood. In addition, while most D–A COFs usually display two absorption bands, such spectral signatures disappear in the case of Py-N COF (Fig. 3c),²⁹² TAT-COF (Fig. 3f), and TPB-COF¹⁴¹ where the usual two-band spectrum is replaced by a much broader featureless peak. Finally, unlike the usual assumption that the low (high) energy band can be readily attributed to intermolecular charge transfer (π – π^* transition), our theoretical analysis indicates that both the bands have partial CT character and arise from the efficient mixing between Frenkel- and CT-type excitations.²⁸⁵

As emphasized throughout this section, COFs display exotic photophysical signatures that are extremely sensitive to various factors, including the nature of the building blocks, relative humidity, inter-layer packing arrangement/type of aggregation, particle size, and defect density. UV-vis spectroscopic features significantly vary depending on the type of COF structure (see Fig. 2 and 3). Unlike most COFs that do not display vibronic structure in either of the two bands, NiPc COF exhibits a pronounced vibronic structure in the Q band as shown in Fig. 2a. The spacing between the two vibronic peaks in Fig. 2a is approximately around 1200 cm^{-1} which can be attributed to strong electron–phonon coupling involving the aromatic to quinoidal stretching mode. In order to elucidate structure–photophysics relationships in COFs, it is necessary to develop an in-depth understanding of the factors that govern the

relative intensities of the B and Q bands, the separation between the maximum of the two absorption bands, the broadening of the bands, and the vibronic structure. It is equally important to investigate the role of Frenkel and charge transfer excitons as well as electron–phonon coupling on the photophysical signatures of various COF structures.

Building upon the 3D Holstein polaron model that was recently developed to investigate the effect of defects, domain size, chemical doping, and topology on the mid-IR photophysical signatures and charge transport properties of COFs,^{216,217} future studies will go beyond a simple single chain analysis and focus on developing 3D vibronic exciton models for various COF topologies. Explicit inclusion of intra- and inter-framework electronic interactions, Frenkel and charge separated exciton states, and strong electron–phonon coupling on equal footing is necessary to investigate the spectral changes in both the UV-vis absorption and emission lineshapes of COFs. Furthermore, due to poor crystallinity and high defect density in COFs, it is necessary to incorporate the effects of different forms of structural and conformational defects in future studies.

3.2 Excitons in 2D perovskites

Unlike organic materials where Frenkel and CT excitons are the predominant form of excitations, photoexcitation of hybrid organic–inorganic materials such as 2D perovskites often result in the formation of Frenkel and Wannier–Mott excitons which are associated with the organic and inorganic components, respectively.²⁹⁹ While Frenkel excitons are bound electron–hole pairs localized on a single unit cell, Wannier–Mott excitons are characterized by a much larger Bohr radius and consist of an electron and a hole that can be tens of unit cells or molecules apart.³⁰⁰ Wannier–Mott excitons therefore experience a much smaller Coulomb binding energy (<100 meV) compared to Frenkel excitons ($\approx >500$ meV).³⁰¹ Since 2D perovskites consist of organic and inorganic building blocks, both Frenkel and Wannier–Mott excitons (may) co-exist upon photoexcitation.^{298,302}

The origin of the excitonic fine structure that is observed in the absorption and emission spectra of 2D perovskites^{152,153,218–220,296,297,303} is currently a topic of ongoing debate. Multiple equally spaced peaks are observed in the absorption and emission spectra of $(\text{PEA})_2\text{PbI}_4$ as shown in Fig. 5a and b. Kagan and coworkers attributed the origin of the exciton fine structure, which has a spacing between 40 and 46 meV, to a vibronic progression arising from the coupling of the electronic transition to a distinct vibrational mode located in the organic cation (Fig. 5a).^{152,153,218,297} Similar spacings of 35 meV to 40 meV were observed at low temperature in the measured spectrum for $(\text{PEA})_2\text{PbI}_4$ (Fig. 5c), and were attributed to distinct excitonic peaks by Silva, Srimath, and coworkers.^{219,220} The peak at approximately 40 meV in $(\text{PEA})_2\text{PbI}_4$ have been attributed to Rashba splitting.³⁰⁴ A recent study has attributed the exciton fine structure observed in the photoluminescence spectrum of $(\text{PEA})_2\text{PbI}_4$ to exciton-polaron emission.³⁰⁵



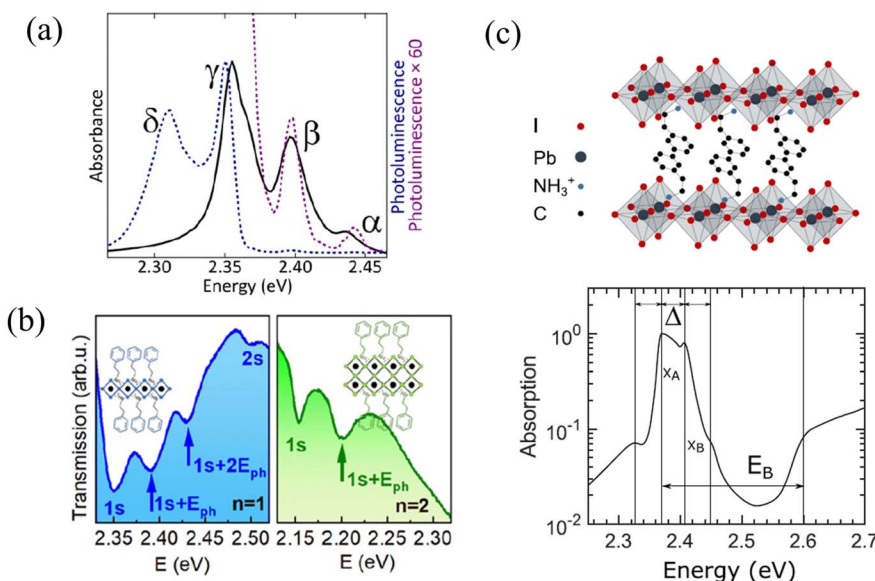


Fig. 5 (a) Exciton fine structure observed in the absorption (solid black) and emission spectrum (dotted black) of phenethylammonium lead iodide.¹⁵² (b) Transmission spectra of $n = 1$ and $n = 2$ thin films of $(\text{PEA})_2(\text{CH}_3\text{NH}_3)_{n-1}\text{Pb}_n\text{I}_{3n+1}$ at 4 K.²⁹⁶ (c) Linear absorption spectrum of $(\text{PEA})_2\text{PbI}_4$ at 5 K.²¹⁹ (a) Reprinted with permission from ref. 152. Copyright 2016 American Chemical Society. (b) Reprinted with permission from ref. 296. Copyright 2020 American Chemical Society. (c) Reprinted with permission from ref. 219. Copyright 2020 American Chemical Society.

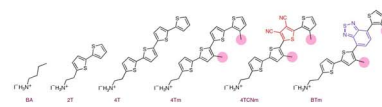
Most perovskites synthesized to date incorporate small organic cations such as methyl-, phenethyl-, or butylammonium as organic spacers. Strauss, Kagan, and coworkers have extensively investigated the role of small organic cations in tailoring the electronic and optical properties of 2D lead halide perovskites.^{153,218,297} The authors demonstrated that single atom substitution on the organic cation dramatically alters the steady-state absorption and emission spectra as shown in

Fig. 6a.¹⁵³ It was also shown that longer organic cations are associated with greater energetic disorder which obscured the presence of the vibronic fine structure in the absorption and emission spectra (Fig. 6b), and resulted in a blue-shifted excitonic absorption.²⁹⁷ Mitzi and coworkers have synthesized perovskites that incorporate oligothiophene cations of various lengths to investigate the role of long and bulky organic components on the photophysical properties of lead halide

(a) Effect of structural deformations



(c) Complex Organic Perovskites



(b) Effect of increasing cation length

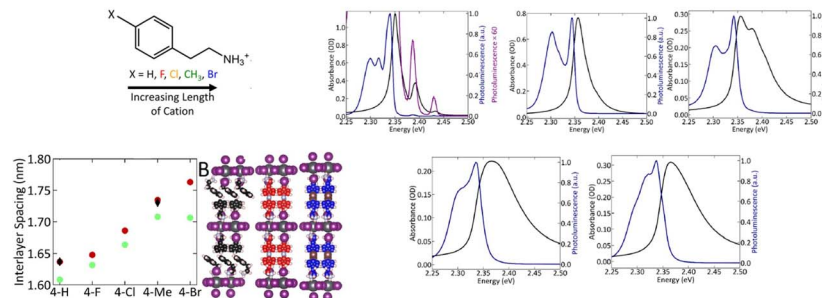


Fig. 6 (a) The exciton fine structure in the UV-vis absorption and emission spectrum in perovskites changes as a function of structural deformation¹⁵³ or (b) increasing length of the organic cations.²⁹⁷ (c) Vibronic progression observed in the UV-vis absorption spectrum of (AE4T)PbI₄.²⁹⁸ (a) Reprinted with permission from ref. 153. Copyright 2020 American Chemical Society. (b) Reprinted with permission from ref. 297. Copyright 2019 American Chemical Society.



perovskites.^{298,306} These perovskites incorporating longer organic cations have been referred to as “complex organic perovskites”.²⁹⁸

Application of the MHF. Spectral signatures of both Frenkel and Wannier–Mott excitons as well as electron–phonon coupling was observed in the absorption spectrum of (AE4T)PbI₄.²⁹⁸ The UV-vis absorption spectrum shown in Fig. 6c exhibits a broad absorption peak centered at ~400 nm which can be directly associated with the Frenkel exciton located in the organic cation.²⁹⁸ The shoulders between 380 nm and 480 nm were attributed to a distinct vibronic progression that arises from the coupling of the Frenkel excitons to the aromatic to quinoidal vibrational mode located in the oligothiophene units. The narrow peak centered at ~520 nm was attributed to the formation of Wannier–Mott excitons.

In order to investigate the UV-vis photophysical signatures associated with the organic layers in (AE4T)PbX₄ perovskites, eqn (1) was expressed for a 2D-herringbone lattice in ref. 242. The eigenstates of the Hamiltonian in eqn (1) was described by a multiparticle basis set by omitting the last term in eqn (8) (since CT excitations are not considered in this study). The unpolarized UV-vis absorption spectrum was obtained using eqn (11). Fig. 7 demonstrates that simulations using the MHF described in ref. 242 accurately reproduce the vibronic progression arising from the organic component in (AE4T)PbX₄ (X = Cl, Br, and I).²⁴² It was also found that the choice of the halide ion in the inorganic component plays a central role in determining the shape of the vibronic structure observed in oligothiophene based perovskites.²⁴² The observed trends in the experimental absorption spectra are a direct consequence of the confining environment provided by the inorganic framework as well as the variation of excitonic coupling that decrease from (AE4T)PbCl to (AE4T)PbI. The theoretical insights gained from ref. 242 are quite relevant in the context of the ongoing debate surrounding the origin of the exciton fine structure. The transition spacings in the excitonic spectra seem to directly correlate with the choice of the organic spacer. While transition spacings of 14 meV and 40 meV were observed in the presence of aliphatic chains^{307,308} and phenyl groups,^{152,219,220,309}

respectively, the presence of oligothiophene cations in (AE4T)PbX₄ results in a distinct progression having a transition spacing equal to the aromatic-to-quinoidal vibrational energy of ≈ 0.17 eV.

Despite rapid progress, several fundamental questions about the optical properties of 2D perovskites still remain unanswered: (a) how do structural changes (*i.e.*, composition, length, and cross-sectional area) induced by the organic cation influence the photophysical properties? (b) What is the physical origin of the excitonic photophysics observed in 2D perovskites at low temperature? (c) How do energetic disorder (in both organic and inorganic layers) and electron–phonon coupling affect the photophysical and transport properties of 2D perovskites? (d) Can spectral signatures be used to distinguish between Frenkel and Wannier Mott excitons in 2D perovskites? While the theoretical model based on the MHF presented in ref. 242 is a promising first attempt to investigate the absorption spectra and gain insights into structure–photophysics relationships in perovskites, future studies need to explicitly include the coupling between Frenkel and Wannier–Mott excitons to further disentangle the role of exciton–exciton coupling in the experimentally measured absorption and emission spectra. We hypothesize that strong organic–inorganic exciton coupling can impact the absorption spectra of perovskites and lead to changes in both the positions and linewidths of the spectral features, as well as changes in the vibronic progression associated with the organic components.

3.3 Excitons in MOFs

UV-vis absorption and emission processes in MOFs are also governed by delocalized excitations.^{129–133,310} Distinct UV-vis spectral signatures similar to what has been discussed for COFs including the coexistence of H- and J-dimer bands³¹¹ have also been observed in MOFs.^{312,313} Extensive research has focused on understanding energy transport pathways and the factors impacting anisotropic exciton migration in MOFs.^{133,134,314–317} Computational and experimental studies have showed that the subtle interplay of several factors like short and long-range excitonic couplings, modular framework structures, and aggregation-induced conformational changes determine the optical properties of MOFs.^{134,226,318–321}

Application of the MHF. Distorted (*i.e.*, non-Franck Condon) vibronic progressions in the photoluminescence spectrum have been observed in SURMOFs.³²⁰ Starting from a non-emissive H-aggregate, the authors used a library of chromophoric MOF linkers to synthesize J-aggregates with bright emission. Super-radiance has been observed in zirconium-based MOFs, namely, PCN-222(Zn), NU-1000, and SIU-100.

As demonstrated in previous sections, the Frenkel–Holstein model described in eqn (1) and (4) is ideally suited to investigate how the interference between long-range Coulomb coupling and short-range superexchange contributions influence the absorption and emission signatures in MOFs.²¹⁵ More importantly, earlier applications of the Frenkel–Holstein Hamiltonian to homopolymers like P3HT, polyacetylene (PDA), and MEH-PPV showed that the UV-vis PL spectral line shape provides

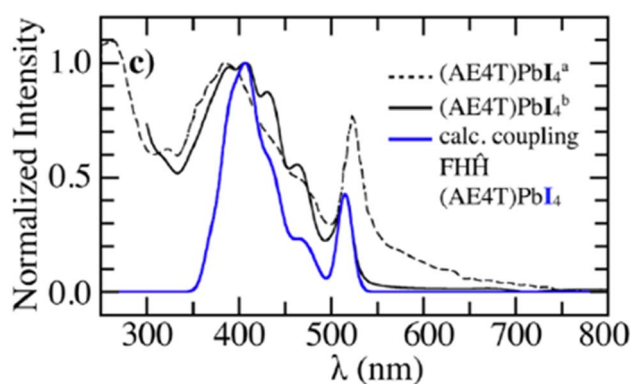


Fig. 7 Comparison of the simulated spectrum using the MHF²⁴² with the measured UV-vis absorption spectrum of (AE4T)PbX₄ from ref. 298. Reproduced from ref. 242, with the permission of AIP Publishing.



direct information about the exciton coherence number,^{278,322} N_{coh} , *i.e.*, the number of repeat units over which the exciton retains wave-like behavior in J-aggregates. In its simplest manifestation, the ratio of 0–0 and 0–1 PL line strengths is given by³²³

$$\frac{I^{0-0}}{I^{0-1}} = \frac{N_{\text{coh}}}{\lambda^2} \quad (13)$$

where λ^2 is the Huang–Rhys factor corresponding to a given repeat unit. The 0–0 peak in the vibronic progression is sensitive to exciton coherence: for example in J-aggregates the 0–0 peak scales linearly with N_{coh} , leading to enhanced radiative decay rates, also referred to as superradiance. Eqn (13) can be effectively used to derive PL signatures which inform on exciton coherence lengths in MOFs. This theoretical analysis will serve as effective screening agent for MOFs with superior light/energy harvesting properties and conversion applications.¹³³

4 Photophysics of polarons

4.1 Polarons in COFs

“Hole” polarons in COFs can be generated by chemical doping with electron withdrawing groups such as iodine or F4TCNQ. Formation of “hole” polarons in COFs results in the appearance of new peaks in the mid-IR energy region. The characteristic mid-IR polaron signatures include a low-energy peak dressed

with infrared active vibrational (IRAV) modes between 0.05 and 0.2 eV, and a broader high-energy peak between 0.25 and 0.9 eV. Such spectroscopic signatures have been observed in iodine-doped imine-linked TANG COF.⁶⁴ Oxidation of COFs also result in near-IR transitions between 1.2 and 2.0 eV. Near-IR signatures have been observed in iodine and F4TCNQ doped WBDT COF,⁶⁵ iodine doped TTF COFs,^{63,329} and electrochemical doping of Py-ttTII COF.²⁹²

Unlike COFs, infrared signatures in conjugated polymers have been extensively investigated as a function of molecular weight, crystallinity of the sample, type of dopant, and preferential location of the dopant molecule. Similar to COFs, creation of polarons in semiconducting homo-polymers and donor-acceptor copolymers, either by photoexcitation (*i.e.*, photoinduced absorption spectroscopy, see Fig. 8b) or by doping (electrochemical or chemical), results in the appearance of new mid-IR peaks. The low-energy peak (see Fig. 8a) has been referred to as peak A,^{229–231,250} DP₁ (delocalized polaron),^{330,331} or CT (charge transfer)^{332–335} by different groups. The broader high-energy peak has been referred to as peak B (Fig. 8a),^{229–231,250} P₁,^{330,331} or C₁.^{332–335}

Effect of chemical doping. Chemical doping has proved to be an excellent strategy for improving conductivity in organic materials. Similar to semiconducting polymers,^{336,337} COFs exhibit up to ten-fold increase in electrical conductivity upon

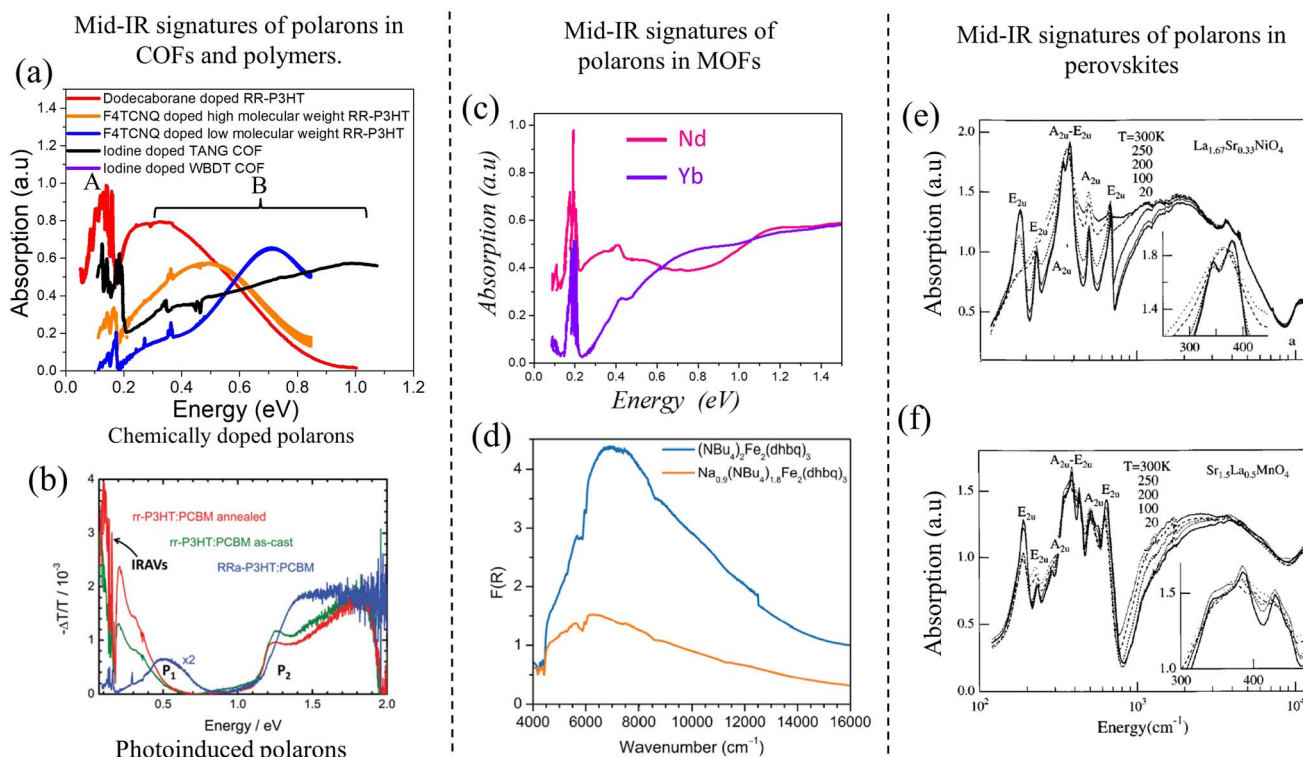


Fig. 8 (a) Mid-IR signatures of “bound” polarons in chemically doped polymers^{230,231} and COFs^{64,216} using data from ref. 216, 230 and 231. A red shift of the high energy peak B signifies enhanced polaron delocalization. (b) Mid-IR signatures of photoinduced polarons in conjugated polymers.^{324,325} (c) and (d) Mid-IR signatures of polarons in MOFs.^{326,327} (c) Replotted from ref. 326. (d) Reprinted with permission from ref. 327. Copyright 2015 American Chemical Society. (e) and (f) Mid-IR signatures of polarons in perovskites.³²⁸ Copyright 1996 by American Physical Society. All rights reserved.



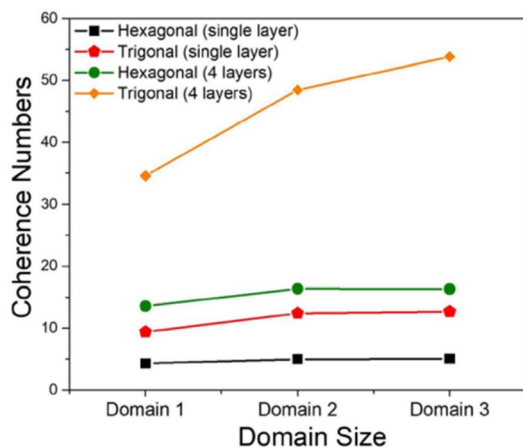


Fig. 9 Intra- and inter-framework polaron coherence numbers as a function of topology of the COF structure. Trigonal COFs facilitate greater polaron delocalization compared to hexagonal COFs due to additional connecting pathways that help circumvent deep trap states and enhance hole mobility. Data is used from ref. 217.

prolonged exposure to iodine.^{63–72} For example, iodine doping significantly increased the conductivity of TANG-COF from $1.6 \times 10^{-5} \text{ S cm}^{-1}$ to $1.0 \times 10^{-2} \text{ S cm}^{-1}$ in vacuum.⁶⁴ This sharp increase in conductivity was associated with an increase in the number of free spins and the emergence of the A and B polaron peaks in the mid-IR energy range (Fig. 10a). Formation of free charge carriers was also observed in iodine-doped tetrathiafulvalene (TTF) COFs which resulted in high conductivity ($2.8 \times$

$10^{-5} \text{ S cm}^{-1}$).^{63,66,329} The increase in conductivity in TTF-ph COF was associated with increased delocalization of the polarons along the inter-layer π -stacking directions.

Effect of location, size, and type of dopant counterion on conductivity. Despite significant progress, most COFs exhibit lower conductivity compared to doped polythiophenes. To readily appreciate the nature of polaron trapping and the origin of poor conductivity in iodine doped COFs, it is important to compare and contrast the mid-IR signatures of iodine-doped TANG-COF with earlier studies on doped conjugated polymers (Fig. 8a). This comparison will facilitate a much deeper understanding of the correlations among mid-IR spectral signatures, dopant type, dopant location, polaron delocalization lengths, and conductivity in COFs.

We begin the discussion with F4TCNQ-doped low molecular weight (MW) P3HT films, where the polarons are localized on the polymer backbones with negligible interchain delocalization.²³⁰ This is due to strong Coulomb binding with the F4TCNQ counteranions that reside in the amorphous domains in close proximity to the polymer backbone (within $\sim 0.5\text{--}0.6 \text{ nm}$). Localized polarons in low-MW F4TCNQ-doped P3HT films correspond to a blue-shifted peak B maximum ($\sim 0.7 \text{ eV}$) and a small A/B peak intensity ratio (~ 0.25 in Fig. 8a). In marked contrast, F4TCNQ-doped high-MW P3HT films display enhanced intra- and inter-chain polaron delocalization which is accompanied by a red shift of the B peak to $\sim 0.5 \text{ eV}$ and an increase in the A/B peak ratio to ~ 0.5 (orange curve in Fig. 8a). The enhanced polaron delocalization in F4TCNQ-doped high-MW regioregular-P3HT is mainly attributed to weak Coulomb

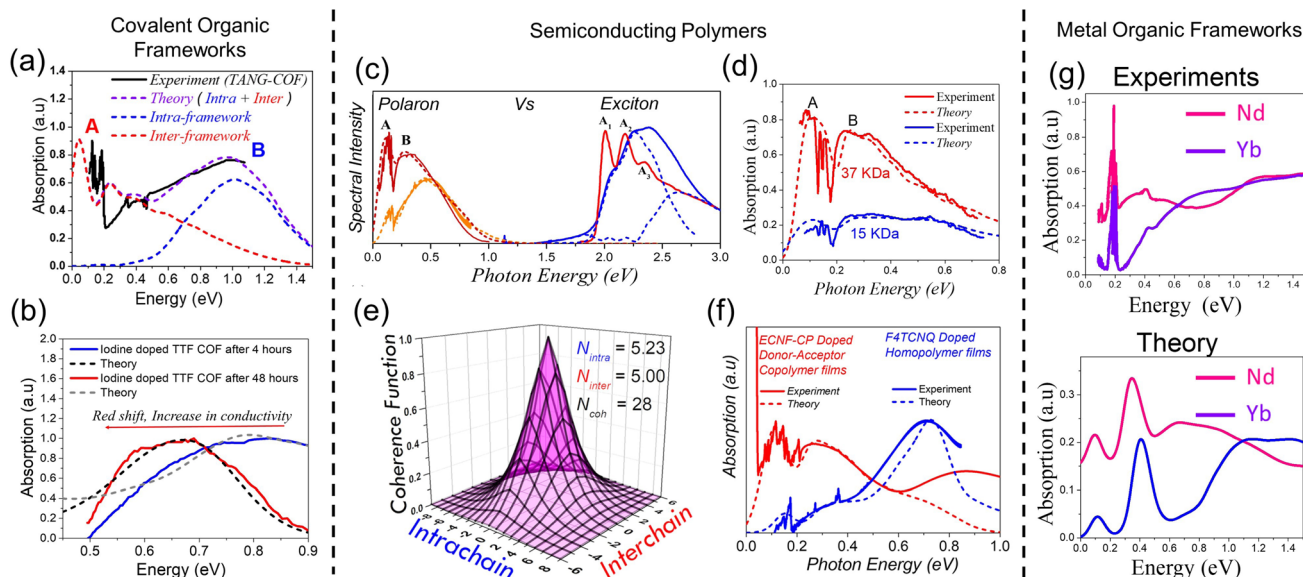


Fig. 10 Measured (solid) and simulated (dashed) spectrum of iodine doped (a) TANG COF and (b) TTF-COFs.^{63,216,217,329} (c) Left: measured (solid) and simulated (dashed) mid-IR polaron spectra of dodecaborane³⁵⁹ (brown) and F4TCNQ²³⁰ (orange) doped P3HT films. Right: measured (solid) and simulated (dashed) exciton UV-vis spectra for undoped P3HT films.^{235,236,250} (d) Measured (solid) and simulated (dashed) charge modulation spectrum of P3HT as a function of molecular weight.²²⁹ (e) Measured (solid) and simulated (dashed) charge modulation spectrum for a doped D–A copolymer³⁴² and P3HT films.^{230,231} (f) Polaron coherence function of 100% regioregular P3HT on a surface assembled monolayer with a molecular weight of 30 kg mol^{-1} . Intra- and inter-chain coherence numbers are shown in the inset.²³³ (g) Preliminary simulations using the MHF qualitatively captures the spectral trends of the mid-IR spectral signatures observed in lanthanide based MOFs replotted from ref. 326. Data in (a)–(f) are from ref. 216, 217, 229–231, 233 and 250.



binding since the dopant counteranions in crystalline high-MW RR-P3HT films preferentially reside in the lamellar regions or in the amorphous domains of the polymer matrix and do not intercalate between the crystalline π -stacks.³³⁸

Interestingly, replacing F4TCNQ dopant with a bulky dodecaborane-based dopant, DDBF₇₂, yielded significantly higher charge mobility in P3HT films, which was accompanied by an additional red shift of the B peak to ~ 0.3 eV and a further increase in the A/B peak intensity ratio to 1.25 (red curve in Fig. 8a). The increased mobility in DDBF₇₂-doped P3HT films³³⁹ compared to F4TCNQ-doped P3HT films²³⁰ is a direct consequence of increased polaron delocalization due to reduced electrostatic interactions between the dopant counteranion and the hole. Unlike F4TCNQ dopants, the reduced Coulomb binding in dodecaborane based dopants was due to a specific design which sterically protected the core electron density.³³⁹

For iodine-doped TANG-COF, the black curve in Fig. 8a display a significantly blue-shifted B peak with the maximum at ~ 1 eV. As expected, this large blue shift correlates to the iodine-doped TANG-COF exhibiting lower conductivity compared to semiconducting polymers and is a direct consequence of localized polarons due to “very” strong Coulomb binding. In the case of polymers, the counteranions preferentially reside at a distance greater than 0.5 nm from the backbone depending on the size of the dopant counteranion and the MW of the polymer films. However, the presence of large pores in TANG-COF (and other COF structures) readily incorporates the counteranions, which results in shorter counteranion-framework distances (0.35–0.4 nm).²¹⁶ In turn, this leads to polaron trapping and, consequently yields lower conductivity.

These studies imply that the preferential location, type, and size of the dopant counteranion play an important role in determining conductivity of 2D COFs and 1D polymers. For example, the Brinkmann group investigated the effects of different dopants on the charge transport properties of P3HT films.³⁴⁰ It was found that the preferential doping of the amorphous regions of the polymer films reduces polaron localization and improves charge transport as well as thermoelectric factors. Similar conclusions were reached from a systematic analysis of the effects associated with the counteranion size on polaron delocalization and mid-IR spectral signatures.³⁴¹

Effect of topology. Both exciton and polaron migration in COFs depend on the topological connectivity or lattice symmetry. Using a topology-templated polymerization strategy, the Jiang group successfully synthesized a series of fully sp^2 carbon-conjugated COFs having hexagonal, tetragonal, and kagome topologies.³⁴ The investigation of π -conjugation effect led to the important conclusion that the extent of exciton migration was controlled by lattice topology with an order of kagome > tetragonal > hexagonal. Similar trends have been observed for polaron migration where HBC COF having trigonal topology exhibits higher mobility compared to other COFs having different topologies.³⁴

Application of the MHF. Fig. 10a and b show that the Holstein-type Hamiltonian (eqn (4)), represented in a multiparticle basis set (first two terms in eqn (8)), and modified to include defects (eqn (9)), quantitatively reproduces the mid-IR

spectral signatures of iodine doped “bound” polarons in TANG-COF and TTF-COFs.²¹⁶ In our current theoretical framework, a near-IR peak corresponds to a HOMO–LUMO transition and requires a more complex multiexcitation Hamiltonian than what is shown in eqn (1). Hence, analysis of near-IR transitions is not further considered. In earlier studies, the MHF has quantitatively reproduced the mid-IR signatures of chemically doped “bound” polarons as well as electrically and optically generated “free” polarons in homopolymers and D–A copolymers, prepared under a variety of conditions, allowing us to establish unambiguous structure-photophysics-transport relationships (Fig. 10c–f).^{229–234,250,338,339,342}

The theoretical analysis identifies specific spectral signatures from which the polaron coherence lengths along the intra- and inter-chain/framework directions in conjugated polymers and COFs can be quantitatively determined. More specifically, direct signatures of extended polaron coherence in conjugated polymers^{229–231,250} and COFs^{216,217} can be attributed to a red shift of the high energy peak B and an increase in the A/B peak intensity ratio. Knowing the coherence distribution is critical since it allows for determining whether charge transport in organic materials is limited by a nanoscale property, such as polaron delocalization, or a mesoscale property, such as crystallite connectivity.²³³

The quantitative theoretical treatment of the infrared signatures in chemically doped organic materials (Fig. 10) provides additional information about how the size, type, and preferential location of the dopant counteranions within the polymer matrix impacts conductivity. As discussed previously, simulations based on the MHF have predicted the approximate location of the counteranion in F4TCNQ-doped and DDBF₇₂-doped P3HT films to be within ~ 0.8 – 1 nm (ref. 230) and ~ 1.8 – 2.0 nm (ref. 231 and 339) of the polymer backbone, respectively. For iodine doped TANG-COF, it was shown that the counteranions reside inside the pore at an approximate distance of ~ 0.35 – 0.50 nm from the COF framework.²¹⁶

The MHF in eqn (1) was used to theoretically demonstrate that the extent of polaron migration along the intra- and interframework directions follows the order trigonal/kagome > tetragonal > hexagonal.²¹⁷ It was theoretically demonstrated that polaronic transport in COF structures not only depends on the extent of π -conjugation and the strength of electronic coupling between the nearest neighbors but is also governed by the interplay between topological connectivity and presence of electronic defects in the framework. Ref. 217 further emphasized that the presence of additional connecting pathways in trigonal COFs compared to hexagonal COFs helps circumvent deep trap sites and significantly enhances polaron delocalization by approximately three orders of magnitude (Fig. 9).²¹⁷ However, this conclusion does not hold in the case of doped COF structures. Upon chemical doping, the effect of topology is virtually nullified and the extent polaron delocalization is primarily determined by the location of the counteranion relative to the COF backbone and the strength of Coulomb binding. In the likely scenario of the dopant counteranions residing inside the COF pores and in close proximity to the framework



backbone, the extent of polaron delocalization, and conductivity will be low, independently of the framework topology.²¹⁷

4.2 Polarons in MOFs

Direct correlations between mid-IR signatures and conductivity is not limited to organic materials, such as polymers and COFs, but have also been reported in hybrid organic–inorganic frameworks, such as MOFs.^{326,327,343–346} A recent study demonstrated that π – π stacking interactions between the organic ligands alone can produce efficient charge transport pathways in MOFs, indicating that a metal–ligand bond with high covalent character is not a necessary requirement for achieving high conductivity.³²⁶ By fine-tuning the inter-layer π -stacking distances between the organic 2D sheets in a series of lanthanide-based MOFs, the measured conductivity was found to be on par with the highest conductivity values reported for MOFs to date. The high conductivity was achieved despite negligible in-plane electronic communication and was solely attributed to out-of-plane charge transport. Although electronic structure calculations were used to determine the band structure and density of states of lanthanide-based MOFs, it would be important to further explore, at the fundamental level, the relationships between framework properties (*e.g.*, flexibility and chemical nature of the organic ligands), measured conductivities, and mid-IR spectral signatures. Firstly, it is quite intriguing that a small decrease (0.005 nm) in the inter-layer stacking distance results in a significant increase (10^3) in the measured conductivity. Secondly, determining the origin of the mid-IR spectral features was deemed beyond the scope of the work and the origin of the mid-IR signatures was ambiguously assigned either to the presence of defects or metal/ligand vacancies and intra-ligand charge transfer (Fig. 8c). Interestingly, similar to the case in organic materials, spectral changes in the mid-IR energy range measured in ref. 326 directly correlate with changes in the inter-layer stacking distances, choice of the metal centers, and measured conductivity. In particular, it was found that frameworks containing metals such as holmium (Ho^{3+}) and ytterbium (Yb^{3+}), which exhibit shorter π -stacking distances and higher conductivities, display a blue-shifted absorption (at ≈ 0.7 eV) compared to frameworks containing lanthanum (La^{3+}) and neodymium (Nd^{3+}), which exhibit longer π -stacking distances and lower conductivities (see Fig. 8c and ref. 326).

Direct correlations between measured conductivity and mid-IR signatures were also reported in $\text{K}_x\text{Fe}_2(\text{BDP})_2$ ($\text{BDP}^{2-} = 1,4$ -benzenedipyrazolate) by Long and coworkers.³⁴⁵ It was shown that the fractional reduction of $\text{K}_x\text{Fe}_2(\text{BDP})_3$ results in a remarkable 10^4 fold increase in conductivity along a single crystallographic axis. It was also found that the greatest degree of electronic delocalization occurred at half reduction, resulting in a charge mobility of $0.29 \text{ cm}^2 \text{ V}^{-1} \text{ s}^{-1}$. With increasing reduction and charge mobility, the spectral features in the mid-IR energy range between 0.50 eV and 1 eV were found to grow in intensity until half reduction and then starts to diminish. The

origin of the mid-IR absorption band was attributed to the formation of mid-gap polaron states.

Direct correlations between mixed valency, conductivity, and mid-IR spectral signatures were also reported in a 3D MOF composed of Fe^{III} centers and paramagnetic semiquinoid linkers synthesized by the Long group.³²⁷ The intense blue curve in Fig. 8d was associated with significantly higher conductivity (0.16 S cm^{-1}) compared to the orange curve (0.0062 S cm^{-1}). However, the underlying physical mechanism behind the difference in spectral intensities was not directly investigated and the observed correlation between spectral intensity and conductivity was not elucidated. Similar low-energy spectral features have been observed in several redox-active MOFs and were either attributed to intra-valence charge transfer or mid-gap polaron states.^{343,344,346}

Application of the MHF. In order to lay the groundwork for future theoretical studies on MOFs, Fig. 10g shows that preliminary calculations carried out for lanthanide-based MOFs using the MHF for polarons (eqn (1)),^{216,217} modified to include defects (eqn (9)) qualitatively reproduces the spectral trends and lineshapes observed in ref. 326. The MHF calculations shown in Fig. 10g were carried out for a hexagonal lattice consisting of four π -stacked layers, and the intra- and inter-framework couplings were set to 0.14 eV and 0.08 eV, respectively. However, the simulated spectrum is blue shifted relative to the measured spectrum and highlights the pitfall for our current theoretical framework (eqn (1)). This discrepancy is likely due to the neglect of the effects associated with the metal centers in the MOF structure. Furthermore, accurate electronic couplings, which can be obtained from DFT calculations, are needed to reliably parameterize the Hamiltonian in eqn (1). In this regard, the development of computational approaches for accurate calculations of the nearest-neighbor electronic couplings in hybrid materials such as MOFs are currently in progress.

Important future directions will be aimed at understanding, at a fundamental level, the origin of the low-energy spectral features in MOFs, which can be tentatively assigned to intra-ligand charge transfer or the formation of delocalized polarons, most probably in the organic ligands. The decrease in spectral intensity observed for 3D MOFs in ref. 327, which is accompanied by a decrease in conductivity, is in good agreement with our earlier observations for COFs^{216,217} and semi-conducting polymers,^{229,230,250} suggesting that the observed drop in mid-IR oscillator strength is directly proportional to the decrease in the polaron delocalization lengths in the MOF structures. However, detailed theoretical investigations are necessary for developing a consistent picture of the correlations between mid-IR signatures and polaron delocalization in different MOF structures.

4.3 Polarons in perovskites

Studies of mid-IR absorption spectra on chemically doped perovskites date back to the 90s.^{328,347} The correlations between the polaronic features in the mid-IR energy range and the transport properties and superconductivity were established in



layered perovskites in ref. 328 and 347. The spectral intensity and lineshapes of the mid-IR signatures were shown to be sensitive to polaron size, doping, and temperature. The similarity between the mid-IR signatures observed in chemically doped layered perovskites having general formula $\text{La}_{2-x}\text{Sr}_x\text{MO}_4$ ($M = \text{Ni}, \text{Mn}, \text{and Cu}$) and those observed in COFs, MOFs, and conjugated polymers is particularly striking.

The mid-IR band of perovskites also display two main bands – a high-energy broad peak (peak B) and a low-energy peak (peak A) riddled with IRAV modes. Although not discussed by the authors, the position of peak B appears to correlate with the transport property of the perovskite structure. For example, $\text{La}_{2-x}\text{Sr}_x\text{NiO}_{4+y}$ (LSNO) either turns into a high temperature superconductor or displays metallic behavior, while $\text{Sr}_{2-x}\text{La}_x\text{MnO}_4$ (SLMO) remains insulating at any value of x . The metallic behavior in LSNO was associated with a red shift of peak B and the band maximum occurred at 2000 cm^{-1} (Fig. 8e). On the other hand, the band maximum of SLMO is approximately around $\sim 4000 \text{ cm}^{-1}$ (Fig. 8f). In addition, peak A also appears to grow in intensity for LSNO compared to SLMO. These observations suggest that it would be important to connect specific spectral signatures of polarons, bipolarons, and polaron pairs with the nature of transport in perovskites (*i.e.*, superconducting *vs.* insulating).

5 Conclusion

To summarize, this perspective highlights a successful theory based on the Holstein Hamiltonian, coined Multiparticle Holstein Formalism, that accounts for the steady-state UV-vis absorption (and PL) spectrum for excitons and the mid-IR spectrum for polarons in a broad range of organic and organic–inorganic hybrid materials. More importantly, the theory identifies specific spectral signatures in the UV-vis and mid-IR that directly correlates with the extent of exciton and polaron coherence in semiconducting materials.

With regards to excitons in organic materials such as COFs and polymers, we show that the incorporation of Frenkel and CT electronic states as well as vibronic coupling are necessary to accurately reproduce the UV-vis absorption spectral line shape of neutral (*i.e.* undoped) D–A polymers such as PffBT4-2DT²⁸⁵ and D–A COFs such as py-ptII²⁹³ (see Fig. 4). The close agreement between theory and experimentally measured UV-vis spectra led to the important conclusion that the origin of the Q and B bands in D–A polymers and D–A COFs arise due to efficient mixing between Frenkel and CT states.

The striking similarity in the low energy vibronic signature of PffBT4-2DT copolymer and NiPc COF have been highlighted. More specifically, both PffBT4-2DT copolymer and NiPc COF display a red-shifted low-energy absorption band which is accompanied by an increase in the A_1/A_2 peak ratio (see Fig. 2a), where A_1 and A_2 are the oscillator strengths of the first two vibronic peaks in the progression sourced by the symmetric aromatic to quinoidal vibrational mode. Although referred to as pure H-aggregates, the vibronic signatures indicate that NiPc COF exhibit J-type aggregation. Examples of H- and J-type bands in COFs have been discussed in Section 3.1 and the importance

of short-range (or superexchange) coupling, which arises from wave function overlap between neighboring chromophores in understanding aggregate photophysics for polymers and COFs have been emphasized.

Section 3.1 demonstrates that the UV-vis spectral signatures of D–A COFs are quite sensitive to molecular packing, nature of aggregation, defect density, relative humidity, and oxidation. From a theoretical viewpoint, future studies based on the MHF will explore whether the interplay between short- and long-range couplings and defects can be exploited in designing superior electrochromic, light-harvesting, and conductive COFs.

With regards to excitons in layered perovskites, the MHF adopted in ref. 242 has successfully reproduced the spectral trends in the vibronic progression observed in the UV-vis absorption spectra of AE4TPbX₄. In ref. 242, the interaction between the organic and inorganic excitons in AE4TPbX₄ was assumed to be negligible. In order to provide an unambiguous interpretation of the excitonic photophysics in layered perovskites, future studies will explicitly include the coupling between Frenkel and Wannier–Mott excitons. To realize this goal, the behavior of the inorganic excitons can be described with a Wannier–Mott type Hamiltonian that accounts for electron and hole hopping, as well as Coulomb binding. Analogous to the studies that have been previously performed on organic materials,²²⁷ we believe that a generic theoretical framework that treats the coupling between Frenkel and Wannier–Mott excitons, electron–phonon coupling associated with both the organic and inorganic components, respectively, and different forms of electronic and structural defects on equal footing will potentially enable direct comparisons with excitonic signatures in hybrid materials.^{152,153,218,219,297}

In the context of polarons, we emphasize that the mid-IR signatures that arise due to the formation of polarons, contain key information about structure–property relationships and the extent of polaron delocalization for both organic and hybrid materials. In our earlier studies^{216,217,229–231,250} (see Fig. 10) we have successfully employed the MHF for polarons (see Section 2.3) to obtain converged and accurate reproductions of the mid-IR absorption spectra of chemically-induced holes as well as electrically and optically-generated holes in homopolymers, D–A copolymers, and COFs. More importantly, the theory provides direct correlations between infrared spectral changes and experimentally measured trends in conductivity and hole mobility. Building upon quantitative fits with available experimental data for both polymers and COFs, we attempt to bridge the gap between the polymer and COF communities by addressing two key questions. (1) What is the fundamental reason for doped COFs to show lower bulk conductivity compared to doped conjugated polymers? (2) Is it possible to identify experimental protocols that can lead to superior conductivity in COFs? In Section 4 and in ref. 216 we demonstrate that strong Coulomb binding between the hole and the counter-anion that resides within the COF pores results in poor conductivity in COFs. As discussed in Section 4 and in ref. 216 and 217, potential design strategies to improve electrical conductivity in COFs involve: (i) the exploration of bulky



dopants and synthesis techniques that preferentially keeps the counteranions away from the COF pores thus reducing Coulomb binding and facilitating enhanced polaron delocalization, and (ii) improving topological connectivity that helps circumvent disorder induced deep trap sites and greatly enhance polaron delocalization.

While the Holstein Hamiltonian for polarons described in eqn (1) quantitatively reproduces the infrared signatures in organic materials (Fig. 10a–f), the model only qualitatively captures the spectral trends in MOFs (Fig. 10g) highlighting the limitation of the Hamiltonian described in eqn (1). The main reason for the discrepancy between experiments and theory in Fig. 10g is because the basis set expressing the Hamiltonian in eqn (1) does not include the contribution from the inorganic component. As previously discussed in Section 4, the Hamiltonian in eqn (1) can be extended to include the coupling between the Frenkel and Wannier–Mott excitons in order to provide realistic simulations of the optical properties of excitons and polarons in hybrid materials.

Finally, we believe that the future of materials modeling hinges on the synergistic integration of Holstein-style vibronic Hamiltonians with electronic structure methods and data-driven techniques. This integrated approach will not only advance our fundamental understanding of the excited state processes but also provide unambiguous interpretations of well-defined spectral signatures that remains unexplored to date. Building upon the unparalleled accuracy of the MHF in reproducing conceptually complicated experimental data (see Fig. 4, 7, 10 and ref. 227, 230, 231, 242, 243, 250, 285, 348) it is possible to advance the community's fundamental understanding of quantum phenomena of many-body quantum systems at the nanoscale. Furthermore, the uniqueness of the MHF can be exploited to establish transformative design rules for next generation device architectures for applications including but not limited to charge storage devices, photodetectors, supercapacitors, and electrochromic sensors.

Author contributions

FP and RG designed and wrote the manuscript.

Conflicts of interest

There are no conflicts to declare.

Acknowledgements

This research was supported by the National Science Foundation through grant no. CHE-1704063 and used resources of the Extreme Science and Engineering Discovery Environment (XSEDE), which is supported by the National Science Foundation through grant no. ACI-1053575, and the Triton Shared Computing Cluster (TSCC) at the San Diego Supercomputer Center (<https://doi.org/10.57873/T34W2R>). The software PETSC and SLEPc was used to diagonalize the Hamiltonian.^{349–351}

Notes and references

- C. W. Tang and S. A. VanSlyke, *Appl. Phys. Lett.*, 1987, **51**, 913–915.
- J. H. Burroughes, D. D. Bradley, A. Brown, R. Marks, K. Mackay, R. H. Friend, P. L. Burns and A. B. Holmes, *Nature*, 1990, **347**, 539–541.
- O. Inganäs, *Adv. Mater.*, 2018, **30**, 1800388.
- H. Lee, C. Park, D. H. Sin, J. H. Park and K. Cho, *Adv. Mater.*, 2018, **30**, 1800453.
- P. Cheng and Y. Yang, *Acc. Chem. Res.*, 2020, **53**, 1218–1228.
- L. Zhan, S. Li, X. Xia, Y. Li, X. Lu, L. Zuo, M. Shi and H. Chen, *Adv. Mater.*, 2021, **33**, 2007231.
- L. La Notte, L. Giordano, E. Calabrò, R. Bedini, G. Colla, G. Puglisi and A. Reale, *Appl. Energy*, 2020, **278**, 115582.
- S. Park, T. Kim, S. Yoon, C. W. Koh, H. Y. Woo and H. J. Son, *Adv. Mater.*, 2020, **32**, 2002217.
- D. Li and G. Yu, *Adv. Funct. Mater.*, 2021, **31**, 2100550.
- L. Guo, X. Gu, X. Zhu and X. Sun, *Adv. Mater.*, 2019, **31**, 1805355.
- M. Ding, X. Gu, L. Guo, R. Zhang, X. Zhu, R. Li, X. Zhang, W. Hu and X. Sun, *J. Mater. Chem. C*, 2022, **10**(7), 2507–2515.
- A. Privitera, M. Righetto, F. Cacialli and M. K. Riede, *Adv. Opt. Mater.*, 2021, **9**, 2100215.
- H. Chen, W. Zhang, M. Li, G. He and X. Guo, *Chem. Rev.*, 2020, **120**, 2879–2949.
- S. Yuvaraja, A. Nawaz, Q. Liu, D. Dubal, S. G. Surya, K. N. Salama and P. Sonar, *Chem. Soc. Rev.*, 2020, **49**, 3423–3460.
- M. Kim, S. U. Ryu, S. A. Park, K. Choi, T. Kim, D. Chung and T. Park, *Adv. Funct. Mater.*, 2020, **30**, 1904545.
- W. Shi, Y. Guo and Y. Liu, *Adv. Mater.*, 2020, **32**, 1901493.
- P. C. Chow and T. Someya, *Adv. Mater.*, 2020, **32**, 1902045.
- Z. Li, S. K. Sinha, G. M. Treich, Y. Wang, Q. Yang, A. A. Deshmukh, G. A. Sotzing and Y. Cao, *J. Mater. Chem. C*, 2020, **8**, 5662–5667.
- J. Noh, G.-U. Kim, S. Han, S. J. Oh, Y. Jeon, D. Jeong, S. W. Kim, T.-S. Kim, B. J. Kim and J.-Y. Lee, *ACS Energy Lett.*, 2021, **6**, 2512–2518.
- Y.-F. Liu, J. Feng, Y.-G. Bi, D. Yin and H.-B. Sun, *Adv. Mater. Technol.*, 2019, **4**, 1800371.
- H. Ling, S. Liu, Z. Zheng and F. Yan, *Small Methods*, 2018, **2**, 1800070.
- R. Su, S. H. Park, X. Ouyang, S. I. Ahn and M. C. McAlpine, *Sci. Adv.*, 2022, **8**, eabl8798.
- L. Zhou, A. Wanga, S.-C. Wu, J. Sun, S. Park and T. N. Jackson, *Appl. Phys. Lett.*, 2006, **88**, 083502.
- D. Ji, T. Li, W. Hu and H. Fuchs, *Adv. Mater.*, 2019, **31**, 1806070.
- J. Jang, Y. Song, D. Yoo, C. K. Ober, J.-K. Lee and T. Lee, *Flexible Printed Electron.*, 2016, **1**, 023001.
- L. Torsi, M. Magliulo, K. Manoli and G. Palazzo, *Chem. Soc. Rev.*, 2013, **42**, 8612–8628.
- A. H. Jalal, F. Alam, S. Roychoudhury, Y. Umasankar, N. Pala and S. Bhansali, *ACS Sens.*, 2018, **3**, 1246–1263.



- 28 A. P. Cote, A. I. Benin, N. W. Ockwig, M. O'Keeffe, A. J. Matzger and O. M. Yaghi, *Science*, 2005, **310**, 1166–1170.
- 29 D. Rodríguez-San-Miguel and F. Zamora, *Chem. Soc. Rev.*, 2019, **48**, 4375–4386.
- 30 X. Chen, K. Geng, R. Liu, K. T. Tan, Y. Gong, Z. Li, S. Tao, Q. Jiang and D. Jiang, *Angew. Chem., Int. Ed.*, 2020, **59**, 5050–5091.
- 31 K. Geng, T. He, R. Liu, S. Dalapati, K. T. Tan, Z. Li, S. Tao, Y. Gong, Q. Jiang and D. Jiang, *Chem. Rev.*, 2020, **120**, 8814–8933.
- 32 S. Kandambeth, K. Dey and R. Banerjee, *J. Am. Chem. Soc.*, 2018, **141**, 1807–1822.
- 33 M. S. Lohse and T. Bein, *Adv. Funct. Mater.*, 2018, **28**, 1705553.
- 34 S. Dalapati, M. Addicoat, S. Jin, T. Sakurai, J. Gao, H. Xu, S. Irle, S. Seki and D. Jiang, *Nat. Commun.*, 2015, **6**, 1–8.
- 35 N. Huang, P. Wang and D. Jiang, *Nat. Rev. Mater.*, 2016, **1**, 1–19.
- 36 F. J. Uribe-Romo, J. R. Hunt, H. Furukawa, C. Klock, M. O'Keeffe and O. M. Yaghi, *J. Am. Chem. Soc.*, 2009, **131**, 4570–4571.
- 37 F. J. Uribe-Romo, C. J. Doonan, H. Furukawa, K. Oisaki and O. M. Yaghi, *J. Am. Chem. Soc.*, 2011, **133**, 11478–11481.
- 38 J. L. Segura, M. J. Mancheño and F. Zamora, *Chem. Soc. Rev.*, 2016, **45**, 5635–5671.
- 39 H. M. El-Kaderi, J. R. Hunt, J. L. Mendoza-Cortés, A. P. Côté, R. E. Taylor, M. O'Keeffe and O. M. Yaghi, *Science*, 2007, **316**, 268–272.
- 40 X. Feng, X. Ding and D. Jiang, *Chem. Soc. Rev.*, 2012, **41**, 6010–6022.
- 41 H. Furukawa and O. M. Yaghi, *J. Am. Chem. Soc.*, 2009, **131**, 8875–8883.
- 42 E. Jin, M. Asada, Q. Xu, S. Dalapati, M. A. Addicoat, M. A. Brady, H. Xu, T. Nakamura, T. Heine, Q. Chen, et al., *Science*, 2017, **357**, 673–676.
- 43 J. W. Colson and W. R. Dichtel, *Nat. Chem.*, 2013, **5**, 453–465.
- 44 R. P. Bisbey and W. R. Dichtel, *ACS Cent. Sci.*, 2017, **3**, 533–543.
- 45 P. J. Waller, F. Gándara and O. M. Yaghi, *Acc. Chem. Res.*, 2015, **48**, 3053–3063.
- 46 H. Yazdani, M.-A. Shahbazi and R. S. Varma, *ACS Appl. Bio Mater.*, 2021, **5**, 40–58.
- 47 R. Xia, X. Zheng, C. Li, X. Yuan, J. Wang, Z. Xie and X. Jing, *ACS Nano*, 2021, **15**, 7638–7648.
- 48 K. Wang, Z. Zhang, L. Lin, K. Hao, J. Chen, H. Tian and X. Chen, *ACS Appl. Mater. Interfaces*, 2019, **11**, 39503–39512.
- 49 Z. Mi, P. Yang, R. Wang, J. Unruangsri, W. Yang, C. Wang and J. Guo, *J. Am. Chem. Soc.*, 2019, **141**, 14433–14442.
- 50 P. Gao, R. Wei, X. Liu, Y. Chen, T. Wu, M. Shi, M. Wang, N. Li and B. Tang, *Chem. Commun.*, 2021, **57**, 5646–5649.
- 51 B. Wang, X. Liu, P. Gong, X. Ge, Z. Liu and J. You, *Chem. Commun.*, 2020, **56**, 519–522.
- 52 M. C. Scicluna and L. Vella-Zarb, *ACS Appl. Nano Mater.*, 2020, **3**, 3097–3115.
- 53 N. Singh, S. Son, J. An, I. Kim, M. Choi, N. Kong, W. Tao and J. S. Kim, *Chem. Soc. Rev.*, 2021, **50**, 12883–12896.
- 54 Q. Fang, J. Wang, S. Gu, R. B. Kaspar, Z. Zhuang, J. Zheng, H. Guo, S. Qiu and Y. Yan, *J. Am. Chem. Soc.*, 2015, **137**, 8352–8355.
- 55 X. Zhan, Z. Chen and Q. Zhang, *J. Mater. Chem. A*, 2017, **5**, 14463–14479.
- 56 S. B. Alahakoon, C. M. Thompson, G. Occhialini and R. A. Smaldone, *ChemSusChem*, 2017, **10**, 2116–2129.
- 57 F. Chang, J. Zhou, P. Chen, Y. Chen, H. Jia, S. M. Saad, Y. Gao, X. Cao and T. Zheng, *Asia-Pac. J. Chem. Eng.*, 2013, **8**, 618–626.
- 58 Z. Li, X. Feng, Y. Zou, Y. Zhang, H. Xia, X. Liu and Y. Mu, *Chem. Commun.*, 2014, **50**, 13825–13828.
- 59 Q. Yang, M. Luo, K. Liu, H. Cao and H. Yan, *Appl. Catal., B*, 2020, **276**, 119174.
- 60 G.-B. Wang, S. Li, C.-X. Yan, F.-C. Zhu, Q.-Q. Lin, K.-H. Xie, Y. Geng and Y.-B. Dong, *J. Mater. Chem. A*, 2020, **8**, 6957–6983.
- 61 Y. Yang, P. Zhang, L. Hao, P. Cheng, Y. Chen and Z. Zhang, *Angew. Chem., Int. Ed.*, 2021, **133**, 22009–22016.
- 62 Z.-C. Guo, M.-L. You, Z.-J. Wang, Z.-F. Li and G. Li, *ACS Appl. Mater. Interfaces*, 2022, **14**, 15687–15696.
- 63 S.-L. Cai, Y.-B. Zhang, A. B. Pun, B. He, J. Yang, F. M. Toma, I. D. Sharp, O. M. Yaghi, J. Fan, S.-R. Zheng, et al., *Chem. Sci.*, 2014, **5**, 4693–4700.
- 64 V. Lakshmi, C.-H. Liu, M. Rajeswara Rao, Y. Chen, Y. Fang, A. Dadvand, E. Hamzehpoor, Y. Sakai-Otsuka, R. S. Stein and D. F. Perepichka, *J. Am. Chem. Soc.*, 2020, **142**, 2155–2160.
- 65 J. M. Rotter, R. Guntermann, M. Auth, A. Mähringer, A. Sperlich, V. Dyakonov, D. D. Medina and T. Bein, *Chem. Sci.*, 2020, **11**, 12843–12853.
- 66 H. Li, J. Chang, S. Li, X. Guan, D. Li, C. Li, L. Tang, M. Xue, Y. Yan, V. Valtchev, et al., *J. Am. Chem. Soc.*, 2019, **141**, 13324–13329.
- 67 M. Souto and D. F. Perepichka, *J. Mater. Chem. C*, 2021, **9**, 10668–10676.
- 68 M. Wang, M. Wang, H.-H. Lin, M. Ballabio, H. Zhong, M. Bonn, S. Zhou, T. Heine, E. Canovas, R. Dong, et al., *J. Am. Chem. Soc.*, 2020, **142**, 21622–21627.
- 69 Y. Yue, H. Li, H. Chen and N. Huang, *J. Am. Chem. Soc.*, 2022, **144**, 2873–2878.
- 70 X. Xu, S. Wang, Y. Yue and N. Huang, *ACS Appl. Mater. Interfaces*, 2020, **12**, 37427–37434.
- 71 G. Bian, J. Yin and J. Zhu, *Small*, 2021, **17**, 2006043.
- 72 P. Friederich, A. Fediai, S. Kaiser, M. Konrad, N. Jung and W. Wenzel, *Adv. Mater.*, 2019, **31**, 1808256.
- 73 H. Chen, V. V. Ginzburg, J. Yang, Y. Yang, W. Liu, Y. Huang, L. Du and B. Chen, *Prog. Polym. Sci.*, 2016, **59**, 41–85.
- 74 C. Huang, X. Qian and R. Yang, *Mater. Sci. Eng.*, 2018, **132**, 1–22.
- 75 X. Xu, J. Chen, J. Zhou and B. Li, *Adv. Mater.*, 2018, **30**, 1705544.
- 76 B. D. Paulsen, K. Tybrandt, E. Stavrinidou and J. Rivnay, *Nat. Mater.*, 2020, **19**, 13–26.



- 77 Y. Lu, Z.-D. Yu, H.-I. Un, Z.-F. Yao, H.-Y. You, W. Jin, L. Li, Z.-Y. Wang, B.-W. Dong, S. Barlow, et al., *Adv. Mater.*, 2021, **33**, 2005946.
- 78 H. Jin, J. Li, J. Iocozzia, X. Zeng, P.-C. Wei, C. Yang, N. Li, Z. Liu, J. H. He, T. Zhu, et al., *Angew. Chem., Int. Ed.*, 2019, **58**, 15206–15226.
- 79 S. A. Kulkarni, N. Yantara, K. S. Tan, N. Mathews and S. G. Mhaisalkar, *Mater. Today*, 2020, **33**, 122–140.
- 80 Y. Gao, C. Huang, C. Hao, S. Sun, L. Zhang, C. Zhang, Z. Duan, K. Wang, Z. Jin, N. Zhang, et al., *ACS Nano*, 2018, **12**, 8847–8854.
- 81 Y. Liu, J. Cui, K. Du, H. Tian, Z. He, Q. Zhou, Z. Yang, Y. Deng, D. Chen, X. Zuo, et al., *Nat. Photonics*, 2019, **13**, 760–764.
- 82 A. Kojima, K. Teshima, Y. Shirai and T. Miyasaka, *J. Am. Chem. Soc.*, 2009, **131**, 6050–6051.
- 83 M. Yuan, L. N. Quan, R. Comin, G. Walters, R. Sabatini, O. Voznyy, S. Hoogland, Y. Zhao, E. M. Beauregard, P. Kanjanaboos, et al., *Nat. Nanotechnol.*, 2016, **11**, 872–877.
- 84 T. M. Brenner, D. A. Egger, L. Kronik, G. Hodes and D. Cahen, *Nat. Rev. Mater.*, 2016, **1**, 1–16.
- 85 H.-Q. Yin and X.-B. Yin, *Acc. Chem. Res.*, 2020, **53**, 485–495.
- 86 J. Yang and Y.-W. Yang, *Small*, 2020, **16**, 1906846.
- 87 X. Xiao, L. Zou, H. Pang and Q. Xu, *Chem. Soc. Rev.*, 2020, **49**, 301–331.
- 88 K. Asha, K. Bhattacharyya and S. Mandal, *J. Mater. Chem. C*, 2014, **2**, 10073–10081.
- 89 P. Chandra Rao and S. Mandal, *Inorg. Chem.*, 2018, **57**, 11855–11858.
- 90 S. Mandal, S. Natarajan, P. Mani and A. Pankajakshan, *Adv. Funct. Mater.*, 2021, **31**, 2006291.
- 91 M. Lu, Y. Zhang, S. Wang, J. Guo, W. W. Yu and A. L. Rogach, *Adv. Funct. Mater.*, 2019, **29**, 1902008.
- 92 Z. Li, T. R. Klein, D. H. Kim, M. Yang, J. J. Berry, M. F. Van Hest and K. Zhu, *Nat. Rev. Mater.*, 2018, **3**, 1–20.
- 93 A. Mahapatra, D. Prochowicz, M. M. Tavakoli, S. Trivedi, P. Kumar and P. Yadav, *J. Mater. Chem. A*, 2020, **8**, 27–54.
- 94 D. Rambabu, A. E. Lakrachi, J. Wang, L. Sieuw, D. Gupta, P. Apostol, G. Chanteux, T. Goossens, K. Robeyns and A. Vlad, *J. Am. Chem. Soc.*, 2021, **143**, 11641–11650.
- 95 X. Wu, Y. Qiu, Z. Chen, B. Guan, X. Hao, A. I. Rykov, Y. Sun, L. Liu, Y. Zou, J. Sun, et al., *Angew. Chem., Int. Ed.*, 2020, **59**, 20873–20878.
- 96 L. Sun, M. G. Campbell and M. Dincă, *Angew. Chem., Int. Ed.*, 2016, **55**, 3566–3579.
- 97 L. S. Xie, G. Skorupskii and M. Dincă, *Chem. Rev.*, 2020, **120**, 8536–8580.
- 98 M. A. Green, A. Ho-Baillie and H. J. Snaith, *Nat. Photonics*, 2014, **8**, 506–514.
- 99 Y. Rong, Y. Hu, A. Mei, H. Tan, M. I. Saidaminov, S. I. Seok, M. D. McGehee, E. H. Sargent and H. Han, *Science*, 2018, **361**, eaat8235.
- 100 B. R. Sutherland and E. H. Sargent, *Nat. Photonics*, 2016, **10**, 295–302.
- 101 C. Katan, N. Mercier and J. Even, *Chem. Rev.*, 2019, **119**, 3140–3192.
- 102 L. Mao, C. C. Stoumpos and M. G. Kanatzidis, *J. Am. Chem. Soc.*, 2018, **141**, 1171–1190.
- 103 J. L. Mancuso, A. M. Mroz, K. N. Le and C. H. Hendon, *Chem. Rev.*, 2020, **120**, 8641–8715.
- 104 X. Ni, H. Li, F. Liu and J.-L. Brédas, *Mater. Horiz.*, 2022, **9**, 88–98.
- 105 S. Thomas, H. Li, C. Zhong, M. Matsumoto, W. R. Dichtel and J.-L. Brédas, *Chem. Mater.*, 2019, **31**, 3051–3065.
- 106 T. Joshi, C. Chen, H. Li, C. S. Diercks, G. Wang, P. J. Waller, H. Li, J.-L. Brédas, O. M. Yaghi and M. F. Crommie, *Adv. Mater.*, 2019, **31**, 1805941.
- 107 H. Li and J.-L. Brédas, *Chem. Mater.*, 2021, **33**, 4529–4540.
- 108 H. Li, H. Li, S. Xun and J.-L. Brédas, *Chem. Mater.*, 2020, **32**, 9228–9237.
- 109 S. Wang, A. D. Chavez, S. Thomas, H. Li, N. C. Flanders, C. Sun, M. J. Strauss, L. X. Chen, A. J. Markvoort, J.-L. Brédas, et al., *Chem. Mater.*, 2019, **31**, 7104–7111.
- 110 G. Borboudakis, T. Stergiannakos, M. Frysali, E. Klontzas, I. Tsamardinou and G. E. Froudakis, *npj Comput. Mater.*, 2017, **3**, 1–7.
- 111 R. Anderson, J. Rodgers, E. Argueta, A. Biong and D. A. Gómez-Gualdrón, *Chem. Mater.*, 2018, **30**, 6325–6337.
- 112 K. Fabrizio, K. N. Le, A. B. Andreeva, C. H. Hendon and C. K. Brozek, *ACS Mater. Lett.*, 2022, **4**, 457–463.
- 113 S. Chong, S. Lee, B. Kim and J. Kim, *Coord. Chem. Rev.*, 2020, **423**, 213487.
- 114 Z. Shi, W. Yang, X. Deng, C. Cai, Y. Yan, H. Liang, Z. Liu and Z. Qiao, *Mol. Syst. Des. Eng.*, 2020, **5**, 725–742.
- 115 A. Nandy, C. Duan and H. J. Kulik, *J. Am. Chem. Soc.*, 2021, **143**, 17535–17547.
- 116 Q. Tao, P. Xu, M. Li and W. Lu, *npj Comput. Mater.*, 2021, **7**, 1–18.
- 117 R. Lyu, C. E. Moore, T. Liu, Y. Yu and Y. Wu, *J. Am. Chem. Soc.*, 2021, **143**, 12766–12776.
- 118 A. Talapatra, B. P. Uberuaga, C. R. Stanek and G. Pilania, *Chem. Mater.*, 2021, **33**, 845–858.
- 119 J. Kim, D. Kang, S. Kim and H. W. Jang, *ACS Mater. Lett.*, 2021, **3**, 1151–1171.
- 120 A. S. Rosen, J. M. Notestein and R. Q. Snurr, *Curr. Opin. Chem. Eng.*, 2022, **35**, 100760.
- 121 G. A. McCarver, T. Rajeshkumar and K. D. Vogiatzis, *Coord. Chem. Rev.*, 2021, **436**, 213777.
- 122 J. R. Kitchin, *Nat. Catal.*, 2018, **1**, 230–232.
- 123 J. Hwang, R. R. Rao, L. Giordano, Y. Katayama, Y. Yu and Y. Shao-Horn, *Science*, 2017, **358**, 751–756.
- 124 C. Altintas, O. F. Altundal, S. Keskin and R. Yildirim, *J. Chem. Inf. Model.*, 2021, **61**, 2131–2146.
- 125 V. Gladkikh, D. Y. Kim, A. Hajibabaei, A. Jana, C. W. Myung and K. S. Kim, *J. Phys. Chem. C*, 2020, **124**, 8905–8918.
- 126 F. Mayr, M. Harth, I. Kouroudis, M. Rinderle and A. Gagliardi, *J. Phys. Chem. Lett.*, 2022, **13**, 1940–1951.
- 127 C. Chen, Y. Zuo, W. Ye, X. Li, Z. Deng and S. P. Ong, *Adv. Energy Mater.*, 2020, **10**, 1903242.
- 128 J. Li, B. Pradhan, S. Gaur and J. Thomas, *Adv. Energy Mater.*, 2019, **9**, 1901891.
- 129 M. Baranowski and P. Plochocka, *Adv. Energy Mater.*, 2020, **10**, 1903659.



- 130 J.-C. Blancon, A. V. Stier, H. Tsai, W. Nie, C. C. Stoumpos, B. Traore, L. Pedesseau, M. Kepenekian, F. Katsutani, G. Noe, et al., *Nat. Commun.*, 2018, **9**, 1–10.
- 131 M. Dyksik, H. Duim, D. K. Maude, M. Baranowski, M. A. Loi and P. Plochocka, *Sci. Adv.*, 2021, **7**, eabk0904.
- 132 A. H. Proppe, M. H. Elkins, O. Voznyy, R. D. Pensack, F. Zapata, L. V. Besteiro, L. N. Quan, R. Quintero-Bermudez, P. Todorovic, S. O. Kelley, et al., *J. Phys. Chem. Lett.*, 2019, **10**, 419–426.
- 133 S. S. Rajasree, J. Yu, S. M. Pratik, X. Li, R. Wang, A. S. Kumbhar, S. Goswami, C. J. Cramer and P. Deria, *J. Am. Chem. Soc.*, 2022, **144**, 1396–1406.
- 134 L. Cao, Z. Lin, W. Shi, Z. Wang, C. Zhang, X. Hu, C. Wang and W. Lin, *J. Am. Chem. Soc.*, 2017, **139**, 7020–7029.
- 135 J. Yu, R. Anderson, X. Li, W. Xu, S. Goswami, S. S. Rajasree, K. Maindan, D. A. Gómez-Gualdrón and P. Deria, *J. Am. Chem. Soc.*, 2020, **142**, 11192–11202.
- 136 P. Mahato, A. Monguzzi, N. Yanai, T. Yamada and N. Kimizuka, *Nat. Mater.*, 2015, **14**, 924–930.
- 137 A. D. Sample, J. Guan, J. Hu, T. Reese, C. R. Cherqui, J.-E. Park, F. Freire-Fernández, R. D. Schaller, G. C. Schatz and T. W. Odom, *Nano Lett.*, 2021, **21**, 7775–7780.
- 138 H.-J. Son, S. Jin, S. Patwardhan, S. J. Wezenberg, N. C. Jeong, M. So, C. E. Wilmer, A. A. Sarjeant, G. C. Schatz, R. Q. Snurr, et al., *J. Am. Chem. Soc.*, 2013, **135**, 862–869.
- 139 Q. Zhang, C. Zhang, L. Cao, Z. Wang, B. An, Z. Lin, R. Huang, Z. Zhang, C. Wang and W. Lin, *J. Am. Chem. Soc.*, 2016, **138**, 5308–5315.
- 140 N. C. Flanders, M. S. Kirschner, P. Kim, T. J. Fauvell, A. M. Evans, W. Helweh, A. P. Spencer, R. D. Schaller, W. R. Dichtel and L. X. Chen, *J. Am. Chem. Soc.*, 2020, **142**, 14957–14965.
- 141 S. Yang, D. Streater, C. Fiankor, J. Zhang and J. Huang, *J. Am. Chem. Soc.*, 2021, **143**, 1061–1068.
- 142 J. Yin, H. Li, D. Cortecchia, C. Soci and J.-L. Brédas, *ACS Energy Lett.*, 2017, **2**, 417–423.
- 143 L. Zhao, Y. L. Lin, H. Kim, N. C. Giebink and B. P. Rand, *ACS Energy Lett.*, 2018, **3**, 2708–2712.
- 144 N. Keller and T. Bein, *Chem. Soc. Rev.*, 2021, **50**, 1813–1845.
- 145 N. J. Hestand and F. C. Spano, *Acc. Chem. Res.*, 2017, **50**, 341–350.
- 146 F. C. Spano, *Acc. Chem. Res.*, 2010, **43**, 429–439.
- 147 F. C. Spano, *Annu. Rev. Phys. Chem.*, 2006, **57**, 217–243.
- 148 A. D. Wright, C. Verdi, R. L. Milot, G. E. Eperon, M. A. Pérez-Osorio, H. J. Snaith, F. Giustino, M. B. Johnston and L. M. Herz, *Nat. Commun.*, 2016, **7**, 1–9.
- 149 X. Song, C. Peng, X. Xu, J. Yin and H. Fei, *Chem. Commun.*, 2020, **56**, 10078–10081.
- 150 G. Zhang, J. Yin, X. Song and H. Fei, *Chem. Commun.*, 2020, **56**, 1325–1328.
- 151 C. Peng, X. Song, J. Yin, G. Zhang and H. Fei, *Angew. Chem., Int. Ed.*, 2019, **131**, 7900–7904.
- 152 D. B. Straus, S. Hurtado Parra, N. Iotov, J. Gebhardt, A. M. Rappe, J. E. Subotnik, J. M. Kikkawa and C. R. Kagan, *J. Am. Chem. Soc.*, 2016, **138**, 13798–13801.
- 153 D. B. Straus, S. Hurtado Parra, N. Iotov, Q. Zhao, M. R. Gau, P. J. Carroll, J. M. Kikkawa and C. R. Kagan, *ACS Nano*, 2020, **14**, 3621–3629.
- 154 K. M. McCall, C. C. Stoumpos, S. S. Kostina, M. G. Kanatzidis and B. W. Wessels, *Chem. Mater.*, 2017, **29**, 4129–4145.
- 155 J. D. Schultz, J. Y. Shin, M. Chen, J. P. O'Connor, R. M. Young, M. A. Ratner and M. R. Wasielewski, *J. Am. Chem. Soc.*, 2021, **143**, 2049–2058.
- 156 C. Lin, T. Kim, J. D. Schultz, R. M. Young and M. R. Wasielewski, *Nat. Chem.*, 2022, 1–8.
- 157 R. Tempelaar and D. R. Reichman, *J. Chem. Phys.*, 2017, **146**, 174703.
- 158 R. Tempelaar and D. R. Reichman, *J. Chem. Phys.*, 2017, **146**, 174704.
- 159 R. Tempelaar and D. R. Reichman, *J. Chem. Phys.*, 2018, **148**, 244701.
- 160 K. Miyata, F. S. Conrad-Burton, F. L. Geyer and X.-Y. Zhu, *Chem. Rev.*, 2019, **119**, 4261–4292.
- 161 E. A. Arsenault, A. J. Schile, D. T. Limmer and G. R. Fleming, *J. Chem. Phys.*, 2021, **155**, 054201.
- 162 E. A. Arsenault, P. Bhattacharyya, Y. Yoneda and G. R. Fleming, *J. Chem. Phys.*, 2021, **155**, 020901.
- 163 G. D. Scholes and G. R. Fleming, *J. Phys. Chem. B*, 2000, **104**, 1854–1868.
- 164 X. Blase, I. Duchemin and D. Jacquemin, *Chem. Soc. Rev.*, 2018, **47**, 1022–1043.
- 165 X. Blase, I. Duchemin, D. Jacquemin and P.-F. Loos, *J. Phys. Chem. Lett.*, 2020, **11**, 7371–7382.
- 166 N. Bradbury, M. Nguyen, J. R. Caram and D. Neuhauser, arXiv preprint arXiv:2205.06690, 2022.
- 167 A. Ortega-Guerrero, M. Fumanal, G. Capano and B. Smit, *J. Phys. Chem. B*, 2020, **124**, 21751–21760.
- 168 M. Ji, X. Lan, Z. Han, C. Hao and J. Qiu, *Inorg. Chem.*, 2012, **51**, 12389–12394.
- 169 L. Wilbraham, F.-X. Coudert and I. Ciofini, *Phys. Chem. Chem. Phys.*, 2016, **18**, 25176–25182.
- 170 A. R. Kshirsagar, C. Attacalite, X. Blase, J. Li and R. Poloni, *J. Phys. Chem. C*, 2021, **125**, 7401–7412.
- 171 A. R. Kshirsagar, X. Blase, C. Attacalite and R. Poloni, *J. Phys. Chem. Lett.*, 2021, **12**, 4045–4051.
- 172 M. Hussain, X. Song, J. Zhao, Y. Luo and C. Hao, *Mol. Phys.*, 2019, **117**, 823–830.
- 173 T. Feng, D. Streater, B. Sun, K. Duisenova, D. Wang, Y. Liu, J. Huang and J. Zhang, *J. Phys. Chem. Lett.*, 2022, **13**, 1398–1405.
- 174 S. Sun, H.-z. Ma, X. Zhang and Y.-c. Ma, *Chin. J. Chem. Phys.*, 2020, **33**, 569–577.
- 175 A. Molina-Sánchez, *ACS Appl. Energy Mater.*, 2018, **1**, 6361–6367.
- 176 J. Leveillee, C. Katan, L. Zhou, A. D. Mohite, J. Even, S. Tretiak, A. Schleife and A. J. Neukirch, *Phys. Rev. Mater.*, 2018, **2**, 105406.
- 177 X. Zhu, H. Su, R. A. Marcus and M. E. Michel-Beyerle, *J. Phys. Chem. Lett.*, 2014, **5**, 3061–3065.
- 178 G. Giorgi, K. Yamashita and M. Palummo, *J. Phys. Chem. Lett.*, 2018, **9**, 5891–5896.



- 179 C. Quarti, N. Marchal and D. Beljonne, *J. Phys. Chem. Lett.*, 2018, **9**, 3416–3424.
- 180 Y. Cho and T. C. Berkelbach, *J. Phys. Chem. Lett.*, 2019, **10**, 6189–6196.
- 181 Z. Zhang, W.-H. Fang, M. V. Tokina, R. Long and O. V. Prezhdo, *Nano Lett.*, 2018, **18**, 2459–2466.
- 182 M. D. Smith, L. Pedesseau, M. Kepenekian, I. C. Smith, C. Katan, J. Even and H. I. Karunadasa, *Chem. Sci.*, 2017, **8**, 1960–1968.
- 183 B. Monserrat, *J. Condens. Matter Phys.*, 2018, **30**, 083001.
- 184 T. Nelson, S. Fernandez-Alberti, A. E. Roitberg and S. Tretiak, *Acc. Chem. Res.*, 2014, **47**, 1155–1164.
- 185 T. R. Nelson, A. J. White, J. A. Bjorgaard, A. E. Sifain, Y. Zhang, B. Nebgen, S. Fernandez-Alberti, D. Mozyrsky, A. E. Roitberg and S. Tretiak, *Chem. Rev.*, 2020, **120**, 2215–2287.
- 186 W. Li, Y. She, A. S. Vasenko and O. V. Prezhdo, *Nanoscale*, 2021, **13**, 10239–10265.
- 187 P. J. Ollitrault, G. Mazzola and I. Tavernelli, *Phys. Rev. Lett.*, 2020, **125**, 260511.
- 188 D. Mac Kernan, G. Ciccotti and R. Kapral, *J. Phys. Chem. B*, 2008, **112**, 424–432.
- 189 M. Barbatti, *Wiley Interdiscip. Rev.: Comput. Mol. Sci.*, 2011, **1**, 620–633.
- 190 P. Drude, *Ann. Phys.*, 1900, **306**, 566–613.
- 191 P. Drude, *Ann. Phys.*, 1900, **308**, 369–402.
- 192 A. Sommerfeld, *Z. Phys.*, 1928, **47**, 1–32.
- 193 J. Hubbard, *Proc. R. Soc. London, Ser. A*, 1963, **276**, 238–257.
- 194 W. Heisenberg, *Original Scientific Papers Wissenschaftliche Originalarbeiten*, Springer, 1985, pp. 580–597.
- 195 T. Holstein, *Ann. Phys.*, 1959, **8**, 325–342.
- 196 T. Holstein, *Ann. Phys.*, 1959, **8**, 343–389.
- 197 R. Kováčik, S. S. Murthy, C. E. Quiroga, C. Ederer and C. Franchini, *Phys. Rev. B*, 2016, **93**, 075139.
- 198 W. Jiang, X. Ni and F. Liu, *Acc. Chem. Res.*, 2021, **54**, 416–426.
- 199 B. Cui, X. Zheng, J. Wang, D. Liu, S. Xie and B. Huang, *Nat. Commun.*, 2020, **11**, 1–8.
- 200 W. Jiang, S. Zhang, Z. Wang, F. Liu and T. Low, *Nano Lett.*, 2020, **20**, 1959–1966.
- 201 H. Chen, S. Zhang, W. Jiang, C. Zhang, H. Guo, Z. Liu, Z. Wang, F. Liu and X. Niu, *J. Mater. Chem. A*, 2018, **6**, 11252–11259.
- 202 Y. Tanimura, *J. Phys. Soc. Jpn.*, 2006, **75**, 082001.
- 203 A. Ishizaki and G. R. Fleming, *J. Chem. Phys.*, 2009, **130**, 234110.
- 204 B. Kloss, D. R. Reichman and R. Tempelaar, *Phys. Rev. Lett.*, 2019, **123**, 126601.
- 205 I. S. Dunn, R. Tempelaar and D. R. Reichman, *J. Chem. Phys.*, 2019, **150**, 184109.
- 206 M. R. Philpott, *J. Chem. Phys.*, 1971, **55**, 2039–2054.
- 207 F. C. Spano, *J. Chem. Phys.*, 2005, **122**, 234701.
- 208 F. C. Spano, *J. Chem. Phys.*, 2002, **116**, 5877–5891.
- 209 F. C. Spano, *J. Chem. Phys.*, 2003, **118**, 981–994.
- 210 A. Stradomska and P. Petelenz, *J. Chem. Phys.*, 2009, **130**, 094705.
- 211 A. Stradomska and P. Petelenz, *J. Chem. Phys.*, 2009, **131**, 044507.
- 212 M. Hoffmann and Z. Soos, *Phys. Rev. B: Condens. Matter Mater. Phys.*, 2002, **66**, 024305.
- 213 P. Scherer and S. F. Fischer, *Chem. Phys.*, 1984, **86**, 269–283.
- 214 J. Roden, A. Eisfeld and J. S. Briggs, *Chem. Phys.*, 2008, **352**, 258–266.
- 215 D. Dell'Angelo, M. R. Momeni, S. Pearson and F. A. Shakib, *J. Chem. Phys.*, 2022, **156**, 044109.
- 216 R. Ghosh and F. Paesani, *Chem. Sci.*, 2021, **12**, 8373–8384.
- 217 R. Ghosh and F. Paesani, *J. Phys. Chem. Lett.*, 2021, **12**, 9442–9448.
- 218 D. B. Straus and C. R. Kagan, *J. Phys. Chem. Lett.*, 2018, **9**, 1434–1447.
- 219 A. R. Srimath Kandada and C. Silva, *J. Phys. Chem. Lett.*, 2020, **11**, 3173–3184.
- 220 S. Neutzner, F. Thouin, D. Cortecchia, A. Petrozza, C. Silva and A. R. S. Kandada, *Phys. Rev. Mater.*, 2018, **2**, 064605.
- 221 W. K. Haug, E. M. Moscarello, E. R. Wolfson and P. L. McGrier, *Chem. Soc. Rev.*, 2020, **49**, 839–864.
- 222 A. M. Rice, C. R. Martin, V. A. Galitskiy, A. A. Berseneva, G. A. Leith and N. B. Shustova, *Chem. Rev.*, 2019, **120**, 8790–8813.
- 223 S. Xu and Q. Zhang, *Mater. Today Energy*, 2021, **20**, 100635.
- 224 T. Banerjee, F. Podjaski, J. Kröger, B. P. Biswal and B. V. Lotsch, *Nat. Rev. Mater.*, 2021, **6**, 168–190.
- 225 E. A. Dolgoplova, A. M. Rice, C. R. Martin and N. B. Shustova, *Chem. Soc. Rev.*, 2018, **47**, 4710–4728.
- 226 S. S. Rajasree, X. Li and P. Deria, *Commun. Chem.*, 2021, **4**, 1–14.
- 227 N. J. Hestand and F. C. Spano, *Chem. Rev.*, 2018, **118**, 7069–7163.
- 228 L. Gisslén and R. Scholz, *Phys. Rev. B: Condens. Matter Mater. Phys.*, 2009, **80**, 115309.
- 229 R. Ghosh, C. M. Pochas and F. C. Spano, *J. Phys. Chem. C*, 2016, **120**, 11394–11406.
- 230 R. Ghosh, A. R. Chew, J. Onorato, V. Pakhnyuk, C. K. Luscombe, A. Salleo and F. C. Spano, *J. Phys. Chem. C*, 2018, **122**, 18048–18060.
- 231 R. Ghosh, C. K. Luscombe, M. Hamsch, S. C. Mannsfeld, A. Salleo and F. C. Spano, *Chem. Mater.*, 2019, **31**, 7033–7045.
- 232 A. R. Chew, R. Ghosh, Z. Shang, F. C. Spano and A. Salleo, *J. Phys. Chem. Lett.*, 2017, **8**, 4974–4980.
- 233 A. R. Chew, R. Ghosh, V. Pakhnyuk, J. Onorato, E. C. Davidson, R. A. Segalman, C. K. Luscombe, F. C. Spano and A. Salleo, *Adv. Funct. Mater.*, 2018, **28**, 1804142.
- 234 C. M. Pochas and F. C. Spano, *J. Chem. Phys.*, 2014, **140**, 244902.
- 235 J. Clark, C. Silva, R. H. Friend and F. C. Spano, *Phys. Rev. Lett.*, 2007, **98**, 206406.
- 236 E. T. Niles, J. D. Roehling, H. Yamagata, A. J. Wise, F. C. Spano, A. J. Moulé and J. K. Grey, *J. Phys. Chem. Lett.*, 2012, **3**, 259–263.



- 329 S. Jin, T. Sakurai, T. Kowalczyk, S. Dalapati, F. Xu, H. Wei, X. Chen, J. Gao, S. Seki, S. Irle, et al., *Chem.–Eur. J.*, 2014, **20**, 14608–14613.
- 330 R. Österbacka, C. P. An, X. Jiang and Z. V. Vardeny, *Science*, 2000, **287**, 839–842.
- 331 X. M. Jiang, R. Österbacka, O. Korovyanko, C. P. An, B. Horovitz, R. A. Janssen and Z. V. Vardeny, *Adv. Funct. Mater.*, 2002, **12**, 587–597.
- 332 H. Sirringhaus, P. Brown, R. Friend, M. M. Nielsen, K. Bechgaard, B. Langeveld-Voss, A. Spiering, R. A. Janssen, E. Meijer, P. Herwig, et al., *Nature*, 1999, **401**, 685–688.
- 333 J.-F. Chang, J. Clark, N. Zhao, H. Sirringhaus, D. W. Breiby, J. W. Andreasen, M. M. Nielsen, M. Giles, M. Heeney and I. McCulloch, *Phys. Rev. B: Condens. Matter Mater. Phys.*, 2006, **74**, 115318.
- 334 J.-F. Chang, H. Sirringhaus, M. Giles, M. Heeney and I. McCulloch, *Phys. Rev. B: Condens. Matter Mater. Phys.*, 2007, **76**, 205204.
- 335 P. J. Brown, D. S. Thomas, A. Köhler, J. S. Wilson, J.-S. Kim, C. M. Ramsdale, H. Sirringhaus and R. H. Friend, *Phys. Rev. B: Condens. Matter Mater. Phys.*, 2003, **67**, 064203.
- 336 N. Kim, S. Kee, S. H. Lee, B. H. Lee, Y. H. Kahng, Y.-R. Jo, B.-J. Kim and K. Lee, *Adv. Mater.*, 2014, **26**, 2268–2272.
- 337 H. Shirakawa, *Synth. Met.*, 1995, **69**, 3–8.
- 338 D. T. Scholes, P. Y. Yee, J. R. Lindemuth, H. Kang, J. Onorato, R. Ghosh, C. K. Luscombe, F. C. Spano, S. H. Tolbert and B. J. Schwartz, *Adv. Funct. Mater.*, 2017, **27**, 1702654.
- 339 T. J. Aubry, J. C. Axtell, V. M. Basile, K. Winchell, J. R. Lindemuth, T. M. Porter, J.-Y. Liu, A. N. Alexandrova, C. P. Kubiak, S. H. Tolbert, et al., *Adv. Mater.*, 2019, **31**, 1805647.
- 340 Y. Zhong, V. Untilova, D. Muller, S. Guchait, C. Kiefer, L. Herrmann, N. Zimmermann, M. Brosset, T. Heiser and M. Brinkmann, *Adv. Funct. Mater.*, 2022, 2202075.
- 341 E. M. Thomas, K. A. Peterson, A. H. Balzer, D. Rawlings, N. Stingelin, R. A. Segalman and M. L. Chabiny, *Adv. Electron. Mater.*, 2020, **6**, 2000595.
- 342 A. J. Moulé, G. Gonel, T. L. Murrey, R. Ghosh, J. Saska, N. E. Shevchenko, I. Denti, A. S. Ferguson, R. M. Talbot, N. L. Yacoub, et al., *Adv. Electron. Mater.*, 2022, **8**, 2100888.
- 343 P. W. Doheny, J. K. Clegg, F. Tuna, D. Collison, C. J. Kepert and D. M. D'Alessandro, *Chem. Sci.*, 2020, **11**, 5213–5220.
- 344 B. Ding, C. Hua, C. J. Kepert and D. M. D'Alessandro, *Chem. Sci.*, 2019, **10**, 1392–1400.
- 345 M. L. Aubrey, B. M. Wiers, S. C. Andrews, T. Sakurai, S. E. Reyes-Lillo, S. M. Hamed, C.-J. Yu, L. E. Darago, J. A. Mason, J.-O. Baeg, et al., *Nat. Mater.*, 2018, **17**, 625–632.
- 346 M. Yoshizawa, K. Kumazawa and M. Fujita, *J. Am. Chem. Soc.*, 2005, **127**, 13456–13457.
- 347 M. Capizzi, P. Calvani, P. Dore, S. Lupi, P. Maselli, A. Paolone, B. Ruzicka, W. Sadowski and S.-W. Cheong, *Phys. Scr.*, 1996, **196**, 215.
- 348 A. L. Bialas and F. C. Spano, *J. Phys. Chem. C*, 2022, **126**, 4067–4081.
- 349 V. Hernandez, J. E. Roman and V. Vidal, *ACM Trans. Math. Software*, 2005, **31**, 351–362.
- 350 J. E. Roman, C. Campos, E. Romero and A. Tomas, *SLEPC Users Manual*, D. Sistemes Informàtics i Computació, Universitat Politècnica de València Technical Report DSIC-II/24/02 – Revision 3.14, 2020.
- 351 S. Balay, S. Abhyankar, M. F. Adams, J. Brown, P. Brune, K. Buschelman, L. Dalcin, A. Dener, V. Eijkhout, W. D. Gropp, D. Karpeyev, D. Kaushik, M. G. Knepley, D. A. May, L. C. McInnes, R. T. Mills, T. Munson, K. Rupp, P. Sanan, B. F. Smith, S. Zampini, H. Zhang and H. Zhang, *PETSc Web page*, 2019, <https://www.mcs.anl.gov/petsc>.

